Contrib Mineral Petrol (2016) 171:104
DOI 10.1007/s00410-016-1316-y

ORIGINAL PAPER

Geology and genesis of the Toongi rare metal (Zr, Hf, Nb, Ta, Y and REE) deposit, NSW, Australia, and implications for rare metal mineralization in peralkaline igneous rocks

Carl Spandler[1] · **Caitlin Morris**[1]

Received: 6 June 2016 / Accepted: 4 November 2016 / Published online: 19 November 2016

Abstract The Toongi Deposit, located in central NSW, Australia, hosts significant resources of Zr, Hf, Nb, Ta, Y and REE within a small (ca. 0.3 km^2), rapidly cooled trachyte laccolith. Toongi is part of regional Late Triassic to Jurassic alkaline magmatic field, but is distinguished from the other igneous bodies by its peralkaline composition and economically significant rare metal content that is homogenously distributed throughout the trachyte body. The primary ore minerals are evenly dispersed throughout the rock and include lueshite/natroniobite and complex Na–Fe–Zr–Nb–Y–REE silicate minerals dominated by a eudialyte group mineral (EGM). The EGM occurs in a unique textural setting in the rock, commonly forming spheroidal or irregular-shaped globules, herein called "snowballs", within the rock matrix. The snowballs are often protruded by aegirine and feldspar phenocrysts and contain swarms of fine aegirine and feldspar grains that often form spiral or swirling patterns within the snowball. Secondary ore minerals include REE carbonates, Y milarite, catapleiite and gaidonnayite that fill fractures and vesicles in the rock. Based on bulk-rock geochemical and Nd isotope data, and thermodynamic modelling of magma fractionation, the alkaline rocks of the region are interpreted to represent extrusive to hyperbyssal products of mantle-derived magma that ponded at mid-crustal levels (ca. 0.3 GPa) and underwent extensive fractionation under low-oxygen fugacity conditions. The high Na_2O, peralkaline nature of the Toongi Deposit trachyte developed via extensive fractionation of an alkali olivine basalt parental magma initially in the mid-crust and subsequently at shallow levels (ca. 0.1 GPa). This extended fractionation under low fO_2 and relatively low H_2O-activity conditions limited volatile release and allowed build-up of rare metal contents to ore grades. We speculate that the ore minerals may have originally formed from rare metal-rich sodic-silicate melt that formed immiscible globules (subsequently crystallized to EGM) in the magma shortly before emplacement and rapid cooling. Subsequent hydrothermal alteration caused relatively limited and localized remobilization of some ore metals into fractures and vesicles in the rock.

Keywords Peralkaline magma · Rare metal mineralization · Toongi · Crystal fractionation · Liquid immiscibility · Eudialyte · Zirconium

Introduction

The study of lithophile trace elements such as Y, Zr, Nb, Ta and rare earth elements (REE) has greatly facilitated our understanding of many aspects of Earth geochemistry from early Earth evolution (Harrison et al. 2005), solid Earth differentiation and crust formation (Hofmann 1997; Rudnick and Gao 2003), to surface water compositions (Elderfield and Greaves 1982) and surficial environmental processes (Aubert et al. 2002). These elements, also known as rare metals, are also critical economic commodities as they are required for a large range of modern technological applications including medical instrumentation, defence systems,

Communicated by Othmar Müntener.

Electronic supplementary material The online version of this article (doi:10.1007/s00410-016-1316-y) contains supplementary material, which is available to authorized users.

✉ Carl Spandler
carl.spandler@jcu.edu.au

[1] Economic Geology Research Centre, James Cook University, Townsville 4811, Australia

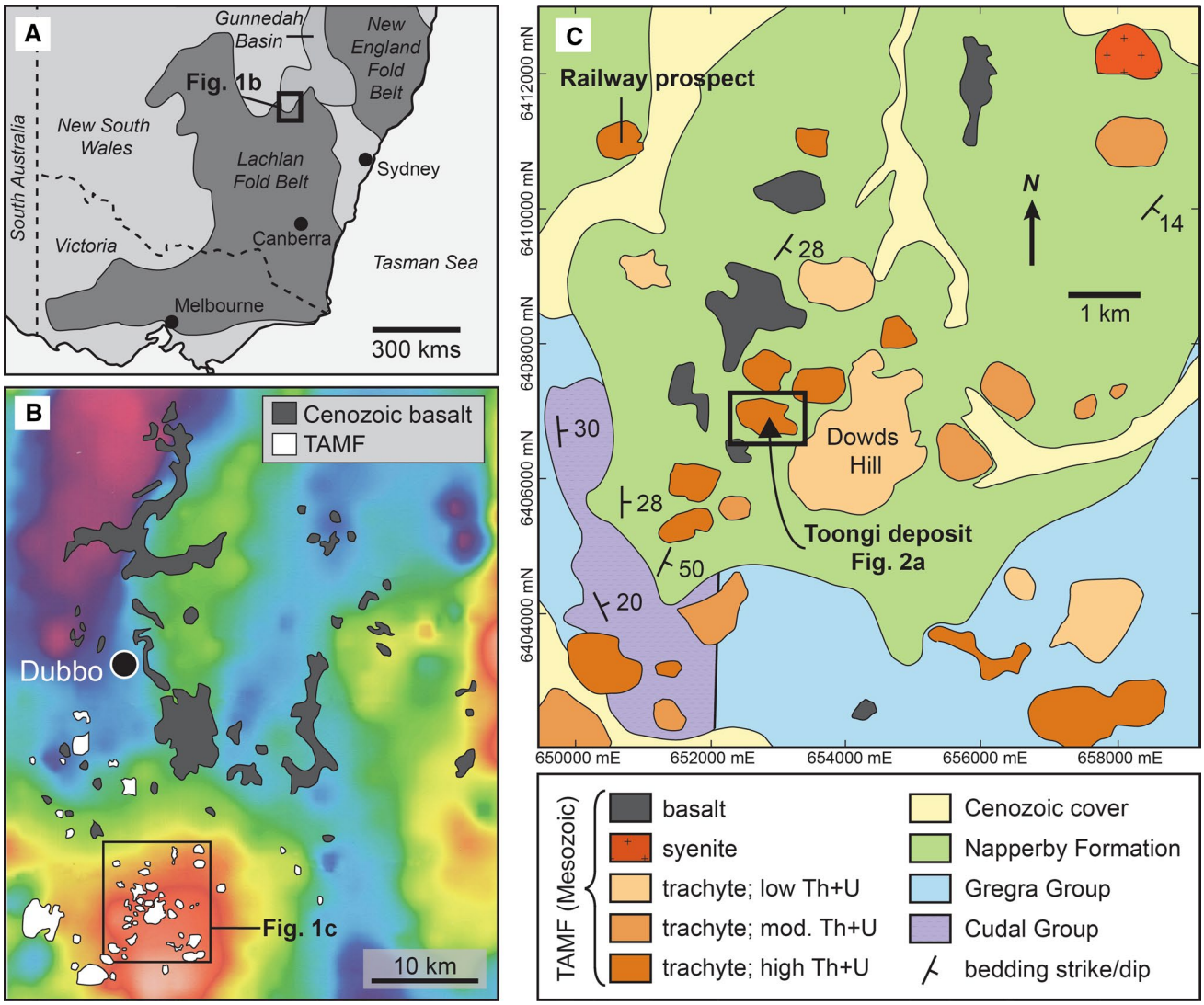

Fig. 1 **a** Relevant basement geology of southeast Australia, with location of Toongi Deposit. **b** Bouguer gravity anomaly map of the Dubbo area overlain by outcropping areas of Cenozoic alkali basalt and TAMF igneous rocks. There is a clear spatial association between the TAMF rocks and the zone of gravity high in the lower left of the image. **c** Geological map of the Toongi Deposit region

high-strength and corrosion-resistant alloys, electronics, and energy generation and storage (e.g. Weng et al. 2015). Nevertheless, despite the growing demand and commercial interest in these metals, our understanding of the geological processes that lead to their concentration to ore grades is rather limited. In most cases, rare metal enrichment can be regarded as a multi-stage process. These elements behave incompatibly during most magmatic processes, so the first step towards ore formation usually involves magma formed as products of extensive fractional crystallization, or by low-degree melting of enriched sources (e.g. Chakhmouradian and Wall 2012). Subsequent upgrading of metal concentration has been attributed to a vast range of processes including—but not limited to—extreme magmatic differentiation (Schmitt et al. 2002; Chakhmouradian and Zaitsev 2012), liquid immiscibility (Thomas et al. 2006; Vasyukova and Williams-Jones 2014), magmatic crystal accumulation (Sheard et al. 2012), hydrothermal and/or metasomatic alteration (Salvi and Williams-Jones 1996; Williams-Jones et al. 2012; Dostal et al. 2014), and weathering and supergene processes (Horbe and da Costa 1999; Chakhmouradian and Wall 2012). These subsequent processes are often essential for obtaining ore grade status, but in general are not well understood.

Arguably the greatest insights into ore formation processes are made from study of actual ore deposits. Here, we present the first detailed geological description of the world-class Toongi multi-rare metal deposit, located approximately 20 km south of the city of Dubbo, New South Wales, Australia (Fig. 1). The Toongi Deposit (also

known as the Dubbo Zirconia Project) contains over 73 Mt of mineral resources (measured and inferred) grading at 1.96 wt% ZrO_2, 0.04 wt% HfO_2, 0.45 wt% Nb_2O_5, 0.03 wt% Ta_2O_5, 0.14 wt% Y_2O_3 and 0.75 wt% REE_2O_3 (Alkane Resources Ltd 2015). Most other major ore deposits with similar metal inventories (e.g. Thor Lake, Strange Lake, Tanbreez; Gysi and Williams-Jones 2013; Sheard et al. 2012; Weng et al. 2015) are hosted by peralkaline intrusive rocks and pegmatites that underwent relatively slow cooling after formation (see also Dostal 2016). By contrast, Toongi is hosted within a small subvolcanic trachytic laccolith that underwent relatively rapid cooling during emplacement. This unusual ore formation setting provides an opportunity to examine primary mineralization features that have been little affected by subsequent subsolidus recrystallization or hydrothermal alteration. This paper outlines the general geological setting and geochemistry of the alkaline igneous rocks of the local area, provides details of the ore textures and mineralogy and discusses magmatic and hydrothermal models for ore formation. These results are not only of significance to the evolution of the Toongi Deposit, but are argued to be more broadly relevant to rare metal ore forming processes in general.

Geological setting

Regional geology

Toongi is one of numerous small alkaline igneous bodies (most are >2 km^2) that collective form a region henceforth called the Toongi Alkaline Magma Field (TAMF; Fig. 1b). The TAMF lies at the boundary between the Permo-Triassic Gunnedah Basin to the north (Meakin and Morgan 1999; Totterdell et al. 2009) and Late Cambrian to Carboniferous Lachlan Fold Belt to the south (Foster and Gray 2000). The basement units in the region (Fig. 1c) include the Late Silurian to Devonian Cudal, Toongi and Gregra Groups of the Lachlan Fold Belt that comprise mixed volcaniclastic and clastic sedimentary sequences with minor rhyolite and limestone (Meakin and Morgan 1999). These units are unconformable overlain by Early-Middle Triassic coarse immature sandstones within interbedded siltstones of the Napperby Formation that is part of the Gunnedah Basin. All of these sedimentary units are host to TAMF igneous bodies.

From the late Triassic to late Jurassic there was widespread, but volumetrically minor, alkaline volcanism across large areas of New South Wales and Victoria (Dulhunty 1967; Meakin and Morgan 1999; McDougall 2008). Zircon fission track and bulk-rock K–Ar dating from the TAMF have returned ages of ca. 170–220 Ma (Meakin and Morgan 1999; Sutherland pers. comm. 2013), confirming a late Triassic to Early Jurassic age of magmatism. Subsequent Cenozoic geological activity in the region includes extensive mafic lava flows now preserved to the north and south of Dubbo city (Zhang and O'Reilly 1997; Fig. 1b) and the development of thin (>4 m) discontinuous alluvium and colluvium. The mafic lavas range in composition from olivine tholeiites, basanites, alkali olivine basalts, hawaiites and mugearites, and are expected to derive from partial melting of both asthenospheric (plume) and subcontinental lithospheric mantle (Zhang and O'Reilly 1997).

Geology of the TAMF

The TAMF comprises approximately 30 relatively small (0.2 to ~10 km^2) elliptical alkaline igneous bodies the outcrop within an area of ca. 200 km^2 to the south of Dubbo. The field is distinguished in regional geophysics as a zone of anomalously high gravity (Fig. 1b) and relatively high Th and U (Meakin and Morgan 1999). The bodies are predominately of trachyte composition, but also include two small syenite intrusions and minor alkali basalts (Fig. 1c); in this paper, we focus on the trachytes and syenites. The trachytes formed at shallow intrusive to extrusive levels as volcanic plugs, laccoliths and lopoliths, flows, and pyroclastic deposits (Fig. 2b; Meakin and Morgan 1999). The trachyte bodies in the immediate vicinity of the Toongi Deposit (Fig. 1c) share many common features. These bodies tend to show concentric zonation, with relatively fine-grained, flow-banded outer margins and relatively homogenous, coarser-grained interiors. Where observable the outer contact of the bodies tends to be sharp, with minor hornfels and quartz veining extending a few metres to 10 s of metres in the country rocks.

The trachytes tend be to fine- to medium-grained and are often vesicular and/or porphyritic, with alkali feldspar phenocrysts ranging in size from several mm to 2 cm. The degree of alteration varies from absent to strong. They may be massive or foliated in outcrop and hand sample, but flow banding in the trachytic matrix is commonly observed in thin section. In general, the trachyte and syenite samples share similar mineral assemblages (excluding the Toongi Deposit, which is described in detail below). They are dominated by alkali feldspar [$K/(K + Na) = 0.5–0.7$], and titanomagnetite, usually with aegirine-augite and/or arfvedsonite (see Electronic Appendix 1) in the groundmass and/or as micro-phenocrysts. Other igneous minerals that form interstitially in the matrix include Mn-rich fayalite, eudialyte, the rare mineral wilkinsonite ($Na_2Fe_6Si_6O_{20}$; see Duggan 1990), and sparse μm-sized zircon and REE-rich apatite. Quartz is rarely present as an igneous phase, but is a major constituent (together with Fe oxides/hydroxides and sericite) of hydrothermal alteration products. Some bodies with elevated rare metal contents (e.g. Railway prospect; Fig. 1c) are extensively silicified and altered.

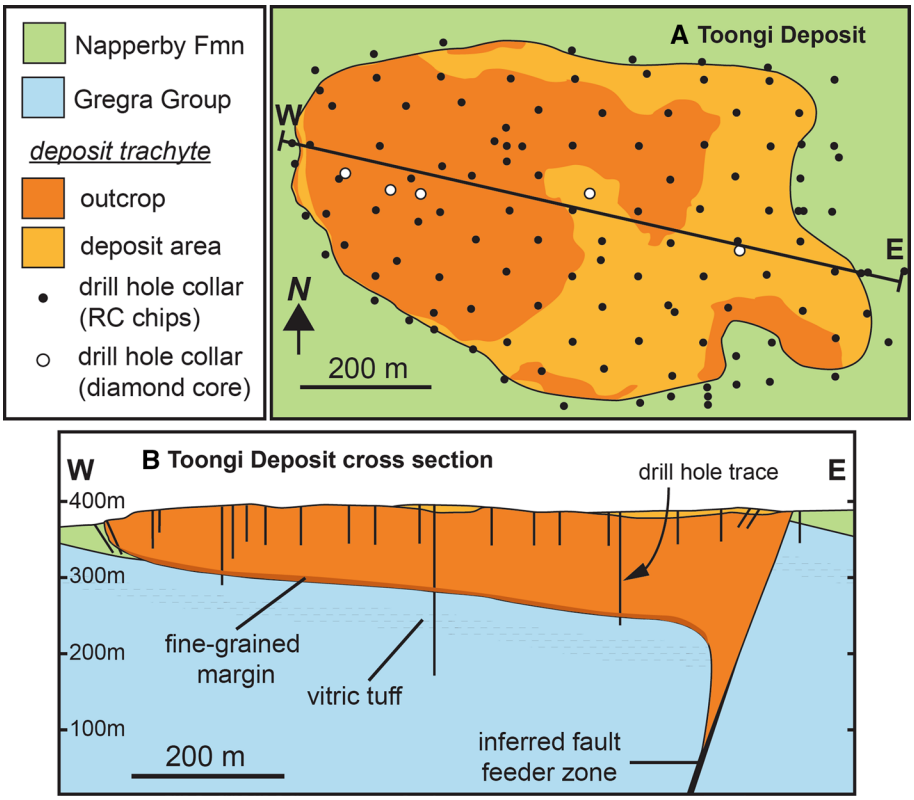

Fig. 2 **a** Geological map of the Toongi Deposit trachyte showing locations of drillhole collars. **b** Interpreted cross section of the Toongi Deposit with drill hole traces, and speculative feeder fault structure

The trachytes bodies are easily recognized by their radiometric signatures (see Meakin and Morgan 1999). Three groups of trachyte bodies are defined (Fig. 1c): (1) A high K, low U, low Th variety (e.g. Dowds Hill; Fig. 1c); (2) high-K, moderate-Th + U ovoid bodies found mainly to the west of Toongi Deposit and (3) high-Th and high-U bodies, which include the Toongi Deposit and Railway prospect. There is little petrographic distinction between rocks of various types, except that some of the high-Th + U trachytes tend to be more intensely altered. Nevertheless, we retain this division of the trachytes for geochemical evaluation, as outlined below.

Geology of the Toongi Deposit

The Toongi rare metal deposit is entirely contained within a ca. 0.3-km^2 elliptical trachyte laccolith located near the centre of the TAMF (Fig. 1c). Zircon fission track dating of the intrusion returned an age of 184 + 19 Ma (Meakin and Morgan 1999). Exploration drilling reveals that the body varies from ~50 m thick in the west to 150 m thick to the east (Fig. 2b). At the surface the deposit is in intrusive contact with the Napperby Formation, whereas the basal contact is with the underlying Gregra Group, and is marked by a fine-grained silicified zone of several metres thickness. The magma feeder structure is not currently recognized; however, based on regional structural trends (see Glen in Meakin and Morgan 1999), we speculate on the existence of a NE-orientated normal fault on the eastern side of the intrusion (Fig. 2b). Although evidence is for such a structure is limited, it would explain the offset of the unit boundaries within the country rocks across the intrusion (Fig. 2b) and may provide a possible feeder structure for the intrusion. Overall, there is very little lithological variation across the intrusion, although flow banding and magmatic brecciation features can be observed in some outcrops and from drillcore. The deposit largely consists of fine-grained (<0.5 mm) trachyte that may be weakly porphyritic and/or vesicular and varies in appearance from cream coloured in the least altered samples, to mottled green to blue-grey with increasing degree of alteration (Fig. 3a). This alteration gives the rock a turbid light brown appearance in thin section.

Up to 10% of the trachyte may consist of 2–4-mm-long elongate vesicles that are horizontally aligned with the magmatic flow foliation. The vesicles are mostly empty voids, but in some cases are partly to completely filled with prismatic quartz and/or a translucent green–brown phase (Fig. 3a) later identified as yttrian milarite (see below). Also sporadically dispersed through the rock are irregular dark blotches up to 1 cm in size (Fig. 3b) that consist of fine-grained Mn oxides (likely pyrolusite) and Mn-rich silicates (likely rhodonite) set within the feldspathic rock matrix.

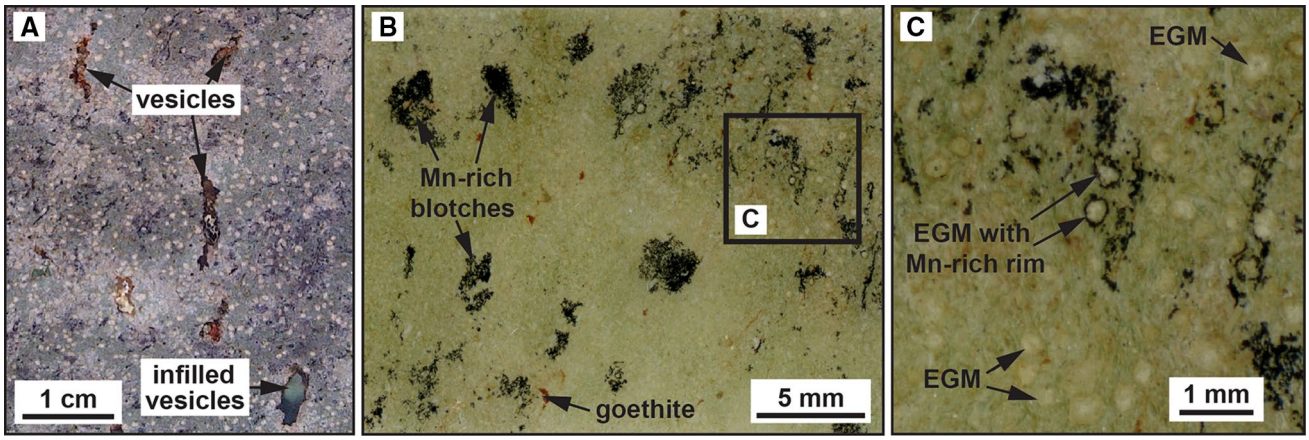

Fig. 3 **a** Photograph of a cut surface of a Toongi Deposit trachyte (drillcore sample TOD3-62.5) with partly filled vesicles. The *colour* variation relates to variable degree of alteration. The fine *cream-coloured* blebs disseminated through the rock are Na–Zr silicate ore minerals. **b** Thin section photograph of Toongi Deposit trachyte (drillcore sample TOD3-57.1) with irregular Mn-rich blotches (*black*). **c** Closer view of Mn-rich zone. Eudialyte group minerals (EGM) are evident as the *cream-coloured spherical* blebs. In some cases, the EGM bleb has an outer rim of Mn oxides

The mineralogy of the Toongi Deposit trachyte differs significantly from other igneous rocks of the TAMF. The intermediate-composition alkali feldspars, primary magnetite, and sodic-calcic pyroxenes and amphiboles that comprise other trachyte and syenite bodies in the area have not been found in the Toongi Deposit. Instead, most of the groundmass and phenocrysts (up to 1 mm) are composed of feldspar that is either near end-member albite or pure K-feldspar in composition (Fig. 4a; Electronic Appendix 1). The phenocrysts are commonly oscillatory zoned, although most phenocryts and groundmass grains have albite rim zones of variable thickness. Textural evidence suggests that these feldspars are of igneous origin, with the exception of the thin albite rim zones that may be of hydrothermal origin. The pyroxene is aegirine (Electronic Appendix 1) and occurs as occasional micro-phenocrysts and as fine (<0.1 mm) acicular crystals as part of the trachytic matrix of the rock (Fig. 4). Arfvedsonite has not been identified, and rare fine-grained quartz may be found interstitial to feldspar and aegirine in the matrix.

The main ore minerals include Na–Ca–Zr silicates, lueshite/natroniobite and REE carbonates that are dispersed throughout the trachyte matrix. The identification, compositions and textural settings of these ore minerals are described in a separate section below.

All of the rock mass has undergone post-magmatic hydrothermal alteration, although the degree of alteration varies considerably, even at the centimetre scale. The most altered samples have pervasive sericite, chlorite and goethite alteration throughout the rock, with only the albitic cores of phenocrysts and aegirine micro-phenocrysts remaining free of alteration.

Extensive drilling and chemical assay of samples of the Toongi Deposit by Alkane Resources Ltd (see Fig. 2a, b) allows delineation of the extent, distribution and variability of ore metals throughout the orebody. The assay data (>4000 1-m composite samples) show that the dimensions of the orebody correspond precisely to the trachyte intrusion volume, with no elevation of rare metal content in the immediate surrounding country rocks (i.e. no mineralization envelope). Moreover, there is a remarkable uniformity in ore metal grades throughout the deposit, with ca. 95% of the rock volume having ore metal concentrations (Nb, Zr, Y and REE) that are within 30% of the mean concentration value (see Fig. 5). There is also no apparent correlation between metal grade and degree of rock alteration. This level of grade homogeneity across the deposit is exceptional when compared to many other ore deposits that tend to have a power law (fractal) distribution between ore grade and mineralized rock volume (e.g. Wang et al. 2010).

Ore mineralogy and textures

The fine grain size, complex textural setting and complex chemistry of most ore minerals in the Toongi Deposit trachyte hampered efforts to identify ore minerals by optical microscope. Therefore, we have undertaken extensive backscattered electron (BSE) imaging and energy-dispersive spectrometry (EDS) using an electron microprobe to characterize ore mineral textures and to aid mineral identification. Most ore minerals could not be precisely identified by EDS alone, and quantitative wavelength-dispersive spectrometry (WDS) proved unreliable due to extreme

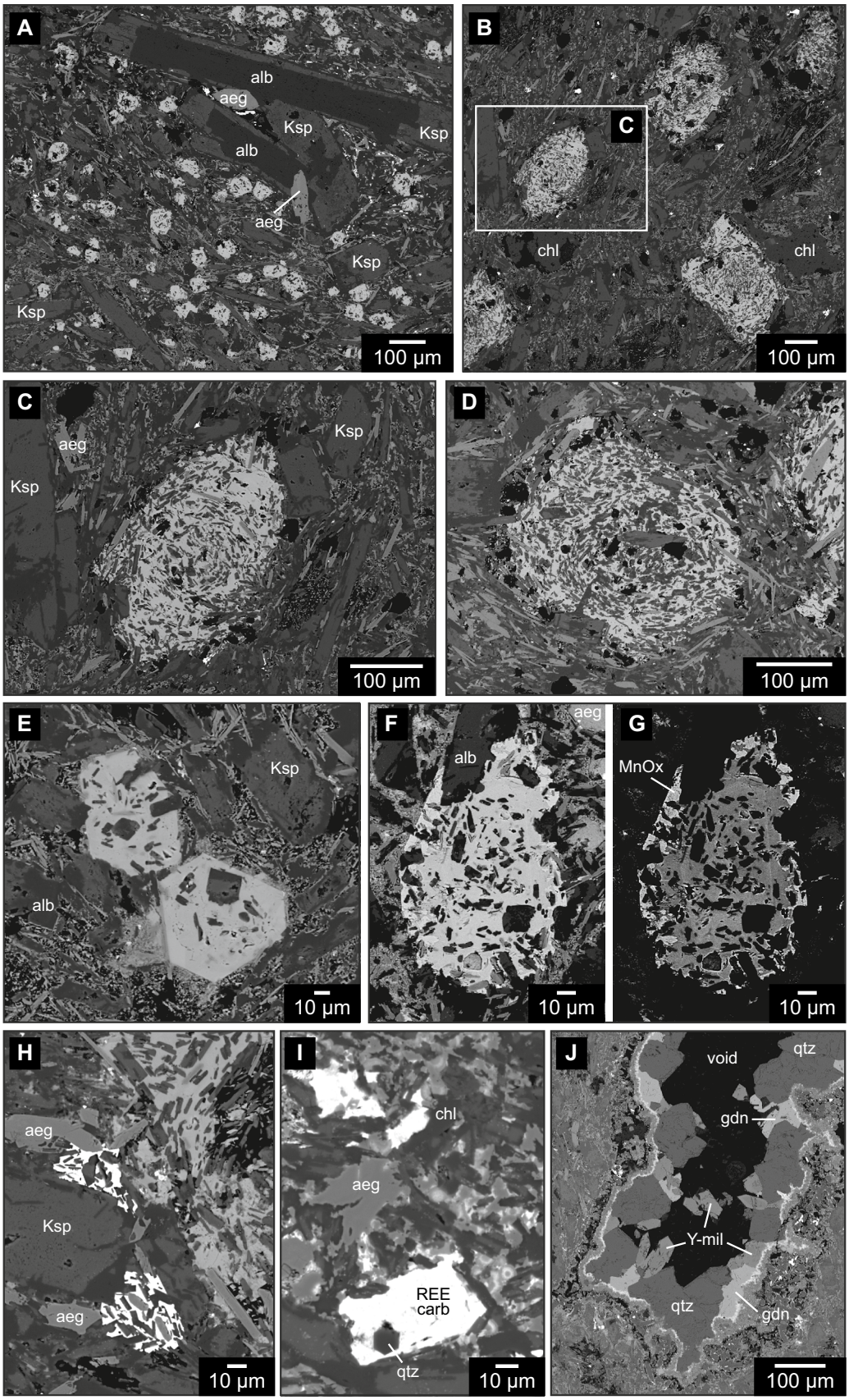
A
alb
aeg
Ksp
Ksp
alb
aeg
Ksp
Ksp
100 µm
B
C
chl
chl
100 µm
C
aeg
Ksp
Ksp
100 µm
D
100 µm
E
Ksp
alb
10 µm
F
aeg
alb
10 µm
G
MnOx
10 µm
H
aeg
Ksp
aeg
10 µm
I
chl
aeg
REE carb
qtz
10 µm
J
void
qtz
gdn
Y-mil
qtz
gdn
100 µm

◂**Fig. 4** Backscatter electron images of ore minerals of the Toongi Deposit. **a** Overview of inclusion-rich blebs of vlasovite (*light grey*) within the trachytic matrix (sample TOD3-108.6). *Note*: the aegirine and zoned feldspar phenocrysts. **b** Snowball eudialyte group minerals (EGM; *light grey*) in sample TOD3-59.0. **c**, **d** Snowball EGM from sample TOD3-59.0 (**c**) and sample TOD3-57.1 (**d**) with irregular grain boundaries and spiral/swirling clusters of feldspar and aegirine inclusions. In some cases, micro-phenocrysts are seen protruding into, or contained within, the EGM grain. **e** Hexagonal catapleiite (*light grey*) in trachytic matrix of sample TOD2-31.1. The catapleiite contains some inclusions of feldspar and aegirine, but much less than the snowball EGM (**c**, **d**). **f**, **g** Snowball EGM associated with Mn-rich blotch from sample TOD3-56.5. Image G is taken under high-contrast conditions to highlight the Mn oxide crystals (*bright grey*) that line the outer surface of the EGM, and the internal zoning of the EGM. The Mn oxides appear to have grown inwards towards the interior of the grain and are interpreted to have grown in a liquid media. **h** Interstitial lueshite/natroniobite (*white*) in sample TOD3-59.0. Note that the lueshite/natroniobite and EGM (*light grey*) appears in textural equilibrium with matrix feldspar and aegirine crystals. **i** Secondary REE carbonates (*white*) with quartz and chlorite from sample TOD3-59.0. *Note*: the ragged and irregular texture of matrix aegirine and feldspar grains, indicating they have undergone reaction and partial dissolution during formation of the secondary ore assemblage. **j** Partially infilled vesicle from sample TOD3-66.9. The outer surface of the vesicles is lined with fine colloform REE carbonates (*white*) and unidentified alkali Zr silicate(s). Prismatic quartz, gaidonnayite and yttrian milarite crystals then grew over the colloform surface into the vesicle void. Mineral abbreviations; *aeg* aegirine, *alb* albite, *Ksp* K-feldspar, *chl* chlorite, *MnOx* Mn oxide, *REE carb* REE carbonate, *qtz* quartz, *gdn* gaidonnayite, *Y-mil* yttrian milarite

instability of some mineral phases under the electron beam (see Electronic Appendix 2 for details), so LA-ICP-MS analysis and Raman spectroscopy were also employed to identify ore mineral species and quantify their chemical composition. Full details of the analytical methods are presented in Electronic Appendix 2.

Examination of samples from across the deposit reveals a remarkable level of uniformity in the mineralogy and textural setting of the ore minerals. The ore minerals are always sub-mm in size and are distributed throughout the rock mass. The bulk of the ore metals are hosted in complex Na–Ca–Zr silicate phases (probably eudialyte, vlasovite and catapleiite) that mainly occur as subspherical to irregular shaped, white to cream coloured blebs (Fig. 3) that are dispersed throughout the rock matrix (Fig. 4a). These phases comprise between 5 and 10% of the rock volume. Their grain size is relatively homogeneous at the millimetre scale, but varies from sample to sample, from sub-50-μm grains, to 200–500-μm grains (compare Fig. 4a, b). In rare cases, these blebs occur in prismatic to hexagonal forms (Fig. 4e). These blebs are interstitial to feldspar and aegirine phenocrysts, and in many cases wrap or include phenocrysts. They are also characterized by an abundance of fine tabular to acicular inclusions of albite, K-feldspar and aegirine that are similar to the rock matrix. These inclusions, or clusters of inclusions, are commonly aligned, and often define spiral or circular forms (Fig. 4c, d) that do not parallel the trachytic flow foliation of the rock matrix. This texture resembles "snowball quartz" described from sodic, rare metal-rich granites from across the globe (e.g. Schwartz 1992; Helba et al. 1997; Müller et al. 2000) and henceforth will be labelled snowball texture. The density of the Na–Ca–Zr silicate blebs tends to be highest in association with the dark patches of Mn oxides and Mn silicates (see Fig. 3c). At these sites, the Na–Ca–Zr silicate blebs often feature an outer zone or carapace of small crystals of Mn oxide (Fig. 3c) that appear to have grown inwards towards the centre of the bleb, as can be seen in Fig. 4g.

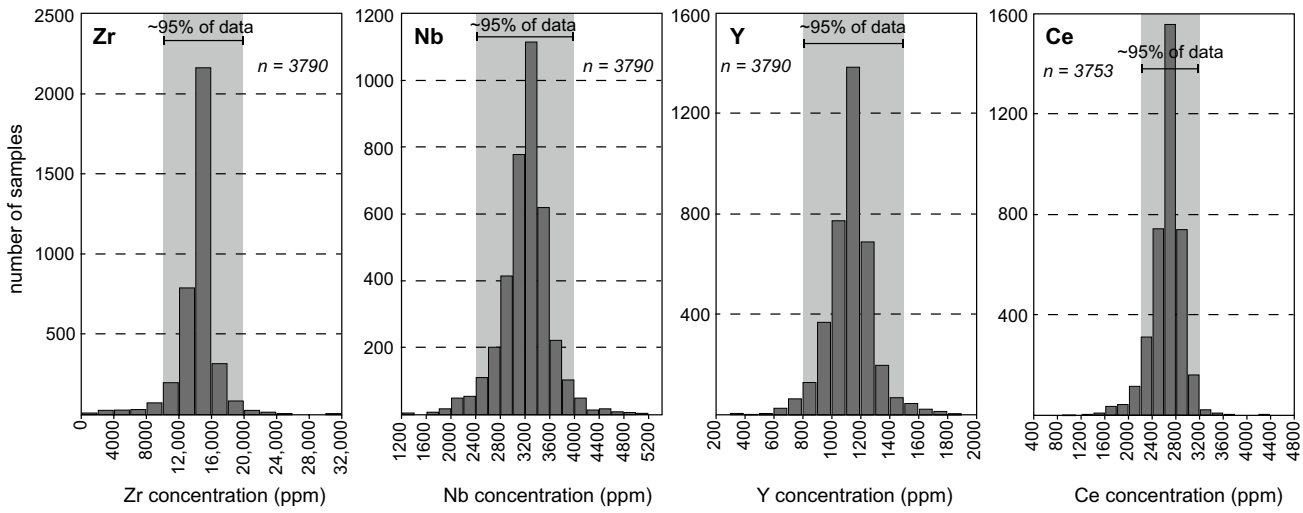

Fig. 5 Histogram of ore element (Zr, Nb, Y and Ce) concentrations from 1-m drillcore composite samples from across the Toongi Deposit. The histograms are used to show that the variation in ore element concentrations is limited throughout the deposit

We have identified three principal Na–Ca–Zr silicate phases that comprise the ore blebs. The most abundant ore phase is a complex Na–Ca–Mn–Fe–REE–Y–Zr–Nb silicate that does not correspond to the composition of any known mineral. Some previous workers have given this phase the obscure label of "zircon gel" (Ramsden 1992). In most cases, this phase lacks crystal habit, contains abundant microscale inclusions and best preserves the snowball textures (Fig. 4c, d). In some rare cases, hexagonal crystal forms or zoning structures are preserved. Raman spectra (532 nm laser) of this phase are characterized by broad peaks at wavenumbers around 550 cm^{-1} and ca. 1000 cm^{-1} (Electronic Appendix 3). We tentatively labelled this phase a Na + Ca-poor, REE-rich eudialyte group mineral (EGM) (Table 1). Members of the eudialyte mineral group span a very broad range of chemical composition (Schilling et al. 2011) and have variable Raman spectral features, but all species feature a prominent Raman peak at wavenumber of ca. 550 cm^{-1} (http://rruff.info) and most tend to have atomic Si/Zr ratio between 7 and 10 (Schilling et al. 2011); both of these features match our data. The phase has low TiO_2, Al_2O_3 and Sr contents, and high MnO (1.5–2 wt%), FeO (5–7 wt%), Nb_2O_5 (~0.8 wt%) and REE + Y (>7 wt%) contents (Table 1; Electronic Appendix 4). Qualitative WDS data indicate this phase has appreciable F (~0.4 wt%) and low Cl (<0.1 wt%) contents.

Based on chemical composition, we have identified two other Na–Ca–Zr–silicate phases that form the ore blebs. Both of these phases are relatively minor compared to the EGM. One phase that forms anhedral to subhedral blocky crystals and has with atomic Si/Zr of ~4 is likely vlasovite ($Na_2ZrSi_4O_{11}$), albeit with variable substitution of Ca for Na (Table 1). The other phase also has variable Na/Ca, but has an atomic Si/Zr of ~3 and often has hexagonal habit (Fig. 4e); this is likely to be a member of the catapleiite mineral group with approximate formula $NaCaZrSi_3O_9{\cdot}2(H_2O)$. Vlasovite contain appreciable Y_2O_3 (~1.5 wt%) and Nb_2O_5 (~3 wt%), and appear in texture equilibrium with rare, fine-grained (<20 μm) REE carbonate that fills interstices between matrix minerals.

The dominant Nb (and Ta) mineral is close to $NaNbO_3$ in composition, and is found as small (<40 μm) irregular grains that also formed in the interstices between matrix feldspar and aegirine grains (Fig. 4h). The phase is either lueshite or the monoclinic equivalent natroniobite. Like the Na–Ca–Zr silicates, these grains can be found throughout the rock matrix and appear in textural equilibrium with surrounding igneous silicate mineral assemblage.

A second assemblage of ore minerals is found infilling vesicles and micro-fractures in the rock. The dominant minerals of this assemblage are irregular REE (fluoro)carbonates that include bastnaesite ($(La,Ce)CO_3F$), Sr-rich galgenbergite ($Sr(La,Ce)_2(CO_3)_2{\cdot}2(H_2O)$) and roentgenite ($Ca_2(La,Ce)_3(CO_3)_5F_3$, with bastnaesite and Sr-rich galgenbergite having both La-rich and Ce-rich compositions (Table 2). These REE carbonates often occur with secondary quartz, and are associated with sericite alteration of feldspar and chloritization of aegirine (Fig. 4i) within the rock matrix, or form thin colloform bands lining vesicles (Fig. 4j). Also associated with REE carbonates are secondary Ca–Na–Zr–silicates that form irregular grains within the rock matrix, or subhedral crystals filling vesicles (Fig. 4j). These phases were identified using Raman and LA-ICP-MS as catapleiite and its polymorph gaidonnayite ($NaZrSi_3O_9{\cdot}2(H_2O)$) (Electronic Appendix 3), or possibly the more hydrated equivalent-phase hilairite ($NaZrSi_3O_9{\cdot}3(H_2O)$). Again, these phases can contain significant amounts of Nb_2O_5 (1–3 wt%; Table 1). The other major vesicle-filling phases are quartz and a Y + REE-rich variant of milarite (Fig. 4j; Electronic Appendix 3), with the approximate formula $KCa_{1.0–1.5}(REE,Y)_{0.5–0.9}BeSi_{12}O_{30}$ (Table 1). These crystals are zoned in REE + Y contents, with some zones having REE + Y contents high enough to qualify for classification as agakhanovite-(Y) (Hawthorne et al. 2014). However, given the substantial variations in REE + Y, this phase is henceforth labelled yttrian milarite. Gaidonnayite, yttrian milarite and quartz can occur together as relatively coarse (up to 0.5 mm) prismatic crystals grown inwards from the vesicle wall (Fig. 4j).

REE geochemistry of ore minerals

Further insights into the origin and paragenetic relationship between ore minerals can be gained from examination of the REE composition of minerals. The EGM have remarkably uniform major and trace element compositions, with slightly LREE-enriched REE patterns that feature a prominent negative Eu anomaly (Fig. 6a). The pattern mirrors the bulk ore REE pattern, albeit with about an order of magnitude higher REE concentration. Vlasovite also has a prominent negative Eu anomaly, but is markedly depleted in LREE relative to HREE, which we suspect is due to co-precipitation with LREE-rich carbonate.

The ore minerals found in fractures and infilling vesicles have a much greater range of REE contents, particularly for the LREE (Fig. 6b). Catapleiite and gaidonnayite have REE patterns that broadly resemble the vlasovite, but have very low LREE contents, which is likely due to sequestration of LREE into coexisting REE (fluoro)carbonates. The REE pattern of yttrian milarite is relatively flat with high contents of MREE (Gd to Er) but relative depletion in La, Tm, Yb and Lu. Catapleiite, gaidonnayite, yttrian milarite and vlasovite all have negative Eu anomalies, but also have distinct positive Y anomalies and overall "m-shaped" REE patterns most clearly characterized by concave down segments

Table 1 Composition of Na–Ca–Zr silicate ore minerals and Y milarite measured by LA-ICP-MS

Sample	TOD3 66.9	TOD3 66.9	TOD3 66.9	TOD3 66.9	TOD3 31.1	TOD3 31.1	TOD3 66.9	TOD3 66.9	TOD3 66.9	TOD3 66.9	TOD3 66.9
Mineral	EGM	EGM	EGM	EGM	Vlasovite	Vlasovite	Catapleiite	Gaidonnayite	Y milarite	Y milarite	Y milarite
Textural setting	Primary, bleb	Primary, bleb	Primary, bleb	Primary, bleb	Primary, bleb	Primary, bleb	Secondary, vesicle	Secondary, vesicle	Secondary, vesicle	Secondary, vesicle	Secondary, vesicle
wt% oxide											
SiO_2	55.61	58.72	54.48	56.34	53.11	51.27	44.22	41.74	70.35	71.54	71.57
Al_2O_3	–	–	–	–	–	–	–	–	1.35	0.55	0.54
FeO	6.14	7.07	5.81	6.22	0.92	0.51	0.93	0.02	–	–	–
MnO	1.62	1.35	1.58	1.54	0.43	0.47	0.58	0.00	0.51	0.42	0.15
CaO	1.85	1.56	1.69	1.72	7.52	8.01	7.36	0.02	5.75	8.16	7.88
Na_2O	9.88	8.52	9.41	8.87	7.25	7.58	7.30	14.46	0.31	0.85	0.65
K_2O	–	–	–	–	–	–	–	–	3.85	3.90	3.92
BeO	–	–	–	–	–	–	–	–	6.95	7.48	7.37
Y_2O_3	1.71	1.43	1.83	1.64	1.46	1.39	0.58	0.37	8.32	4.41	5.00
ZrO_2	14.68	13.96	16.55	15.54	25.84	27.21	26.01	31.93	0.00	0.09	0.06
Nb_2O_5	0.77	0.70	0.86	0.79	2.78	2.85	3.60	1.97	0.00	0.00	0.00
La_2O_3	1.37	1.16	1.39	1.32	0.01	0.01	0.00	0.00	0.03	0.05	0.06
Ce_2O_3	3.10	2.71	3.08	2.91	0.02	0.02	0.00	0.00	0.34	0.62	0.67
Pr_2O_3	0.32	0.28	0.32	0.30	0.00	0.00	0.00	0.00	0.06	0.13	0.14
Nd_2O_3	1.22	1.03	1.24	1.16	0.01	0.01	0.00	0.00	0.32	0.54	0.61
Sm_2O_3	0.29	0.23	0.28	0.26	0.00	0.00	0.00	0.00	0.19	0.25	0.27
Gd_2O_3	0.27	0.22	0.27	0.25	0.00	0.00	0.00	0.00	0.33	0.32	0.32
Dy_2O_3	0.30	0.24	0.30	0.27	0.06	0.06	0.03	0.01	0.74	0.41	0.47
Ho_2O_3	0.06	0.05	0.06	0.05	0.03	0.03	0.00	0.00	0.16	0.08	0.09
Er_2O_3	0.17	0.13	0.17	0.16	0.21	0.20	0.06	0.04	0.45	0.18	0.24
HfO_2	0.25	0.24	0.29	0.27	0.43	0.45	0.31	0.42	–	–	–
F*	0.40	0.40	0.40	0.40	–	–	–	–	–	–	–

Table 1 continued

Molecular formula	Based on Si + Zr + Nb + Hf = 29 cations				Based on 11 oxygens		Based on 9 oxygens		Based on 30 oxygens		
Si	25.52	25.84	25.07	25.39	3.835	3.746	2.953	2.858	11.92	11.96	11.99
Al	–	–	–	–	–	–	–	–	0.269	0.108	0.106
Fe	2.356	2.601	2.236	2.344	0.056	0.031	0.052	0.001	–	–	–
Mn	0.630	0.503	0.616	0.588	0.026	0.029	0.033	0.000	0.073	0.060	0.021
Ca	0.910	0.735	0.883	0.830	0.582	0.627	0.526	0.001	1.044	1.463	1.416
Na	8.791	7.267	8.395	7.749	1.150	1.074	0.945	1.919	0.101	0.276	0.211
K	–	–	–	–	–	–	–	–	0.832	0.832	0.838
Be	–	–	–	–	–	–	–	–	2.827	3.008	2.966
Y	0.417	0.335	0.448	0.393	0.056	0.054	0.021	0.013	0.750	0.393	0.446
Zr	3.286	2.995	3.714	3.415	0.910	0.969	0.847	1.066	0.000	0.005	0.003
Nb	0.160	0.139	0.179	0.161	0.091	0.094	0.109	0.061	0.000	0.000	0.000
La	0.232	0.188	0.236	0.219	0.000	0.000	0.000	0.000	0.002	0.003	0.004
Ce	0.521	0.437	0.519	0.480	0.001	0.001	0.000	0.000	0.021	0.038	0.041
Pr	0.053	0.045	0.054	0.049	0.000	0.000	0.000	0.000	0.004	0.008	0.009
Nd	0.200	0.162	0.204	0.187	0.000	0.000	0.000	0.000	0.019	0.032	0.036
Sm	0.053	0.040	0.051	0.047	0.000	0.000	0.000	0.000	0.013	0.017	0.018
Gd	0.041	0.032	0.041	0.037	0.000	0.000	0.000	0.000	0.019	0.018	0.018
Dy	0.044	0.034	0.044	0.039	0.001	0.001	0.001	0.001	0.040	0.022	0.025
Ho	0.009	0.007	0.009	0.007	0.001	0.001	0.000	0.000	0.008	0.004	0.005
Er	0.025	0.018	0.025	0.023	0.005	0.005	0.001	0.001	0.024	0.010	0.013
Hf	0.033	0.030	0.038	0.035	0.009	0.009	0.006	0.008	–	–	–
Cation total	43.28	41.41	42.76	41.99	6.72	6.64	5.49	5.93	17.97	18.26	18.17

All compositions determined by LA-ICP-MS, assuming 100% totals for eudialyte (including 0.4 wt% F measured by electron probe*), Y milarite and vlasovite. Catapleiite and gaidonnayite were calculated assuming major element totals of 91% to account for a nominal 9% H_2O as per the mineral formula

EGM eudialyte group mineral

Table 2 Composition of REE carbonates from the Toongi Deposit

Sample	TOD3-108.6	TOD3-108.6	TOD3-108.6	TOD3-108.6	TOD3-66.9	TOD3-108.6	TOD3-108.6	TOD3-108.6	TOD3-66.9	TOD3-66.9
Mineral	Bsn (La)	Bsn (La)	Bsn (Ce)	Bsn (La)	Bsn (Ce)	Sr-rich Glg (La)	Sr-rich Glg (Ce)	Sr-rich Glg (La)	Rtg	Rtg
wt% oxides										
CaO	–	–	–	–	–	4.63	4.92	3.68	12.41	12.70
SrO	0.25	0.21	0.07	0.53	0.04	9.98	7.95	12.10	0.00	0.02
La_2O_3	52.90	53.42	30.91	34.47	26.35	34.19	17.42	21.32	14.36	13.98
Ce_2O_3	16.75	17.28	35.24	33.14	36.03	1.68	26.02	20.40	29.63	30.70
Pr_2O_3	1.69	1.52	2.28	2.12	3.06	3.81	3.10	2.95	3.39	3.24
Nd_2O_3	3.52	3.35	5.74	4.67	8.74	10.79	9.24	8.45	10.00	9.41
Sm_2O_3	0.32	0.30	0.52	0.42	0.79	1.08	0.92	0.85	1.00	0.94
F	4.79	5.61	3.43	4.33	3.22	0.00	0.00	0.00	2.87	2.99
H_2O (calc)	–	–	–	–	–	2.88	3.03	3.01	–	–
CO_2 (calc)	20.30	20.48	20.06	20.24	20.10	28.16	29.63	29.37	25.20	25.37
Total	100.52	102.18	98.25	99.92	98.34	97.20	102.23	102.12	98.86	99.35
Molecular formula		Based on 1.5 oxygens					Based on 4 oxygens		Based on 6.5 oxygens	
Ca		–	–	–	–	–	0.51	0.52	0.39	1.91	1.94
Sr		0.01	0.00	0.00	0.01	0.00	0.59	0.45	0.69	0.00	0.00
La		0.70	0.70	0.42	0.46	0.35	1.29	0.63	0.78	0.76	0.74
Ce		0.22	0.23	0.47	0.44	0.48	0.06	0.93	0.74	1.56	1.61
Pr		0.02	0.02	0.03	0.03	0.04	0.14	0.11	0.11	0.18	0.17
Nd		0.05	0.04	0.07	0.06	0.11	0.40	0.32	0.30	0.51	0.48
Sm		0.00	0.00	0.01	0.01	0.01	0.04	0.03	0.03	0.05	0.05
F		1.09	1.27	0.79	0.99	0.74	0.00	0.00	0.00	2.61	2.70
Cation total		1.00	0.99	1.00	1.01	0.99	3.03	2.99	3.04	4.97	4.99

All compositions determined by electron microprobe using wavelength-dispersive spectrometry. Bastnaesite analyses suffered fluorescence effects from neighbouring Ca-bearing carbonates, so the analyses are calculated to be CaO-free. H_2O and CO_2 contents were calculated on the basis of charge balance and best fit to known mineral formulas

Mineral abbreviations: *Bsn* bastnaesite, *Glg* Galgenbergite, *Rtg* roentgenite

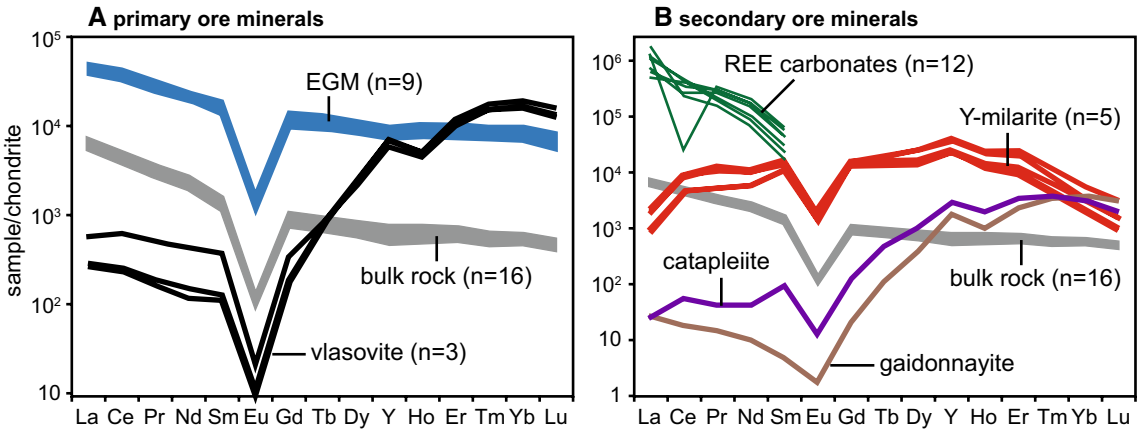

Fig. 6 Chondrite-normalized REE diagrams of **a** primary ore minerals and **b** secondary ore minerals from the Toongi Deposit. *Note*: the EGM have a very similar REE pattern to the bulk-rock samples. Vlasovite, yttrian milarite, gaidonnayite and catapleiite have fractionated Y/Ho and segmented REE patterns that are diagnostic of lanthanide tetrad effects. Chondrite-normalizing values are taken from Taylor and McLennan (1985)

between La and Nd, and between Ho and Lu. These features are characteristic of the lanthanide tetrad effect that is observed in relatively low-temperature magmatic and/or hydrothermal minerals (Bau 1996; Monecke et al. 2011).

Bulk-rock geochemistry

To better understand the source and genetic relationship between igneous rocks of the TAMF, we have undertaken bulk geochemical and Nd isotope analysis of rock samples from across the field area (Fig. 1c). Major and trace element analyses were conducted by XRF and LA-ICP-MS, respectively, and Nd isotope analyses of rock powders were completed by TIMS. Full analytical details are presented in Electronic Appendix 2. Major and trace element, and Nd isotope data are presented in Table 3 and Electronic Appendix 5.

Major/minor elements

The majority of the samples have SiO_2 contents between 60 and 70 wt%, with relatively high alkali ($Na_2O + K_2O$) contents, and plot almost exclusively within the trachyte field of the standard TAS diagram of Le Maitre et al. (2002) (Fig. 7a). A few samples straddle the border with rhyolite/dacite, but these were likely enriched in SiO_2 by hydrothermal alteration, as discussed above. Despite the overall limited range of SiO_2 contents, there are clear major element compositional trend across the suite of rock types. The rocks have relatively low contents of TiO_2, CaO, MgO and P_2O_5, although the low- and moderate-Th + U trachytes and syenites tend to have higher contents of these elements, as well as K_2O, compared to the high-Th + U and Toongi Deposit trachytes (Fig. 7). Most rocks have alumina saturation index (ASI; Al/[Ca − 1.67P + K + Na]; Frost et al. 2001) values of around 1, except for some high-Th + U samples that have lost Na_2O during alteration (Fig. 7c), and the Toongi Deposit trachyte, which has a peralkaline signature [peralkaline index (PI) of 1.4–1.5] with relatively high Na_2O and low Al_2O_3. Compared to the other igneous bodies, the Toongi Deposit trachyte also features elevated Fe_2O_3, low TiO_2 and variable MgO and MnO for the given TiO_2 content. Commonly used fractionation indices for siliceous igneous rocks such as Rb/Ba and the europium anomaly (Eu/Eu*) also directly correlate with TiO_2 content across the igneous suite (Fig. 7h, i).

Our petrographic observations reveal that many of the samples have undergone post-magmatic hydrothermal alteration that manifests most obviously as silica enrichment and Na_2O depletion in some of the high-Th + U samples, including those from the Railway prospect. Many of the most altered samples also have elevated loss-on-ignition (LOI) values (Fig. 8), but there is no significant relationship between LOI and ore metal concentration (Fig. 8b). Excluding the most altered rocks, we do, however, find a direct relationship between bulk-rock Na/Ca of various trachytes, and Na/Ca of their respective alteration-free magmatic pyroxenes (Fig. 8c). This relationship indicates that bulk Na/Ca of most trachytes, including those of the Toongi Deposit, are indicative of their magmatic composition and, hence, have not been significantly modified by alteration.

Ore metals and trace elements

The concentration of the ore metals Zr, Hf, Nb, Ta, Y and REE all positively correlate with all of the alkaline

Table 3 Representative bulk-rock major, trace and Sm–Nd isotope compositions of TAMF rocks

Sample	TOD2-25.8	TOD2-46.2	TOD3-28	TOD3-29.6	TOD3-59.5	TOD3-99.5	TV7	DH1	UG1	GH1	AO1	OM2	C2	RW1	GR2	SHN1	SHN3
Rock type	TD	TD	TD	TD	TD	TD	Low Th + U	Low Th + U	Low Th + U	Med Th + U	Med Th + U	Med Th + U	High Th + U	High Th + U	High Th + U	SYN	SYN
Major elements (in wt% oxides)																	
SiO_2	61.1	60.8	63.07	63.16	61.71	62.8	61.77	66.08	65.17	59.98	61.11	60.43	69.88	69.11	62.74	59.98	60.33
TiO_2	0.08	0.08	0.08	0.09	0.08	0.08	0.26	0.35	0.66	0.12	0.12	0.06	0.12	0.10	0.12	0.37	0.35
Al_2O_3	12.35	12.51	12.62	12.68	12.36	12.24	17.23	15.13	18.23	18.07	17.52	18.43	13.12	11.9	16.22	17.93	18.36
Fe_2O_3	7.49	7.35	7.33	6.71	7.21	7.12	5.9	6.05	2.47	5.12	5.61	4.63	5.77	6.23	5.93	4.54	4.83
MnO	0.28	1.05	0.20	0.30	0.62	0.29	0.18	0.17	< 0.01	0.17	0.19	0.16	0.10	0.27	0.18	0.12	0.12
MgO	0.35	0.17	0.25	0.1	0.11	0.07	0.13	0.14	0.02	0.14	0.07	0.01	0.12	0.11	0.10	0.24	0.24
CaO	0.56	0.48	0.32	0.45	0.34	0.23	1.45	0.26	0.53	1.63	1.44	0.83	0.21	0.07	0.58	1.92	1.67
Na_2O	7.98	8.15	7.4	7.86	8.53	8.47	6.37	4.87	6.10	6.20	7.14	7.99	4.27	2.70	7.33	6.35	6.48
K_2O	4.42	4.29	4.05	4.26	4.25	4.09	5.29	5.06	5.79	5.26	5.13	4.87	3.89	5.21	4.55	5.47	5.59
P_2O_5	0.01	0.01	0.01	0.01	0.01	0.01	0.10	0.10	0.01	0.10	0.10	0.01	0.01	0.09	0.01	0.10	0.10
ZnO	0.22	0.10	0.19	0.23	0.19	0.22	0.02	0.01	0.04	0.02	0.02	0.02	0.06	0.12	0.06	0.01	0.01
Rb_2O	0.15	0.11	0.12	0.15	0.16	0.16	0.01	0.01	0.01	0.03	0.02	0.03	0.06	0.12	0.06	0.01	0.01
Y_2O_3	0.14	0.10	0.11	0.14	0.13	0.13	0.01	0.01	0.01	0.01	0.01	0.01	0.04	0.07	0.03	0.00	0.00
ZrO_2	1.9	1.53	1.60	1.87	1.85	1.83	0.17	0.08	0.09	0.16	0.20	0.20	0.44	0.89	0.48	0.06	0.07
Nb_2O_5	0.47	0.38	0.37	0.49	0.47	0.33	0.03	0.02	0.02	0.03	0.03	0.04	0.14	0.29	0.11	0.01	0.02
La_2O_3	0.20	0.16	0.15	0.20	0.18	0.19	0.01	0.01	0.01	0.02	0.01	0.02	0.02	0.07	0.06	0.01	0.01
Ce_2O_3	0.36	0.29	0.28	0.38	0.34	0.33	0.02	0.01	0.02	0.02	0.03	0.03	0.07	0.12	0.08	0.01	0.01
Nd_2O_3	0.13	0.11	0.10	0.14	0.12	0.12	0.01	0.00	0.01	0.01	0.01	0.01	0.02	0.04	0.03	0.00	0.01
LOI	1.77	1.37	1.12	1.21	1.16	1.07	0.64	1.34	0.54	2.60	0.86	1.86	1.33	2.19	1.06	2.45	1.47
Total	99.96	99.04	99.37	100.43	99.82	99.78	99.60	99.70	99.73	99.69	99.62	99.64	99.67	99.70	99.73	99.58	99.68
Trace elements (in ppm)																	
Be	203	140	221	177	231	191	9.57	4.05	4.29	13.64	12.61	17.32	44.61	49.37	53.31	4.01	5.22
Mg	997	480	671	1528	725	512	1023	1201	330	1139	494	165	1000	464	451	1999	1947
Sc	4.99	4.57	4.03	4.68	4.41	4.29	6.00	4.64	6.71	2.10	3.40	0.82	2.42	1.88	2.68	3.73	3.43
Ti	532	540	587	538	538	518	1566	2360	3326	774	817	409	718	662	756	2406	2231
Cr	26.8	22.1	24.5	23.4	22.1	19.5	24.9	28.0	23.1	76.2	27.9	29.1	20.0	28.1	18.2	31.2	24.3
Mn	7660	608	2317	7554	4405	2044	1292	1239	120	1292	1363	1156	697	1908	1319	862	842
Co	11.39	6.92	12.44	10.07	25.47	12.96	21.43	26.26	35.9	12.23	18.68	18.93	18.24	9.50	23.03	18.99	9.08
Zn	1800	788	1562	1839	1564	1804	143	116	300	130	139	152	491	924	446	69.9	69.7
Ga	161	132	142	164	163	156	35.4	31.1	31.2	32.9	35.4	38.7	70.7	93.9	73.8	22.6	24.1
Rb	1389	968	1122	1335	1469	1444	132	106	115	229	156	283	571	1103	510	101	107
Sr	128	42	45	133	16	6	20.44	16.10	59.3	38.7	10.02	3.35	29.15	14.85	33.7	91.2	111
Y	1141	763	833	1138	1014	987	51.4	52.9	43.9	59.1	53.7	60.1	294	547	233	34.0	34.7
Zr	14033	11,253	11,808	13,816	13,617	13,518	1262	610	628	1162	1486	1496	3215	6591	3517	459	481
Nb	2950	2408	2306	3084	2964	2281	177	105	137	218	216	245	1002	1818	773	98	105

Table 3 continued

Sample	TOD2-25.8	TOD2-46.2	TOD3-28	TOD3-29.6	TOD3-59.5	TOD3-99.5	TV7	DH1	UG1	GH1	AO1	OM2	C2	RW1	GR2	SHN1	SHN3
Rock type	TD	TD	TD	TD	TD	TD	Low Th + U	Low Th + U	Low Th + U	Med Th + U	Med Th + U	Med Th + U	High Th + U	High Th + U	High Th + U	SYN	SYN
Mo	3.73	1.25	1.68	4.06	4.00	2.49	9.55	4.94	4.59	7.44	8	12.74	2.56	1.95	8.55	5.15	11.23
Sn	93	83	99	92	91	90	8.64	6.25	7.93	11.12	10.14	14.03	53.8	91.3	38.6	5.85	5.73
Sb	2.80	3.08	1.87	3.88	1.87	2.68	0.56	0.65	0.53	0.67	0.70	0.70	1.95	2.96	1.06	0.65	0.59
Cs	16.28	3.78	9.83	12.76	14.58	11.98	1.35	1.76	0.70	2.69	2.72	4.33	11.24	4.41	9.68	1.03	1.04
Ba	2.62	18.0	67	98	4.55	2.39	35	118	349	44.0	16.13	3.05	67.5	161	36.9	556	469
La	1688	1346	1306	1747	1584	1593	99	45	76	133	117	149	203	632	484	48.0	48.4
Ce	3057	2488	2414	3278	2924	2872	188	105	154	211	219	240	639	1020	720	92	95
Pr	315	259	250	339	293	297	19.95	11.28	18.32	21.41	21.90	22.32	43.7	110	81.7	9.43	10.37
Nd	1117	916	890	1230	1030	1058	78.7	40.5	73.2	66.6	80.5	65.4	165	357	273	38.3	45.2
Sm	216	174	169	235	195	196	14.02	9.92	13.48	11.49	12.91	11.10	40.0	70.8	46.7	7.61	7.93
Eu	6.29	5.19	4.95	6.76	5.67	5.66	1.20	1.20	1.97	0.67	0.94	0.49	1.25	1.34	1.26	1.62	1.41
Gd	196	152	149	211	175	175	11.43	9.67	10.68	9.90	10.26	9.62	43.2	70.6	40.8	6.77	7.12
Tb	32.2	24.0	24.5	34.2	28.6	28.5	1.72	1.54	1.56	1.55	1.61	1.59	7.68	12.63	6.56	1.05	1.07
Dy	201	145	152	210	177	176	10.25	10.21	9.37	9.37	10.02	10.24	50.7	86.7	41.3	6.32	6.72
Ho	39.5	27.6	29.8	40.6	34.8	33.9	1.94	1.95	1.68	1.86	1.94	2.05	10.11	17.66	8.03	1.23	1.28
Er	109	78	83	109	96	94	5.74	5.87	4.86	5.77	5.94	6.39	28.36	52.3	22.85	3.61	3.85
Tm	15.51	11.48	11.95	15.46	14.07	13.66	0.83	0.80	0.70	0.92	0.91	1.01	4.16	7.96	3.45	0.54	0.56
Yb	91.3	69.9	71.7	90.6	83.6	81.6	5.60	5.63	4.70	5.89	6.16	7.06	25.39	48.9	21.48	3.66	3.75
Lu	12.90	9.94	10.15	12.71	11.70	11.55	0.88	0.83	0.68	0.94	0.97	1.09	3.62	7.12	3.36	0.53	0.57
Hf	307	249	265	302	287	291	24.62	14.34	14.27	23.85	28.99	30.51	93.5	177	84	10.11	10.78
Ta	193	149	142	188	184	153	10.17	6.38	8.34	14.19	13.46	18.54	70.1	108	48.3	5.84	6.05
Pb	205	153	167	199	172	180	10.68	9.48	12.59	15.37	14.26	20.33	72.1	120	44.3	4.89	5.33
Th	400	328	293	388	338	315	16.20	12.20	14.67	28.5	22.21	44.9	101	191	86.7	9.39	9.89
U	73	80	126	120	73	76	5.03	1.51	3.51	6.30	6.71	11.17	23.29	37.4	23.34	2.80	2.96
Nb/Ta	15.28	16.16	16.24	16.40	16.11	14.91	17.44	16.44	16.44	15.34	16.05	13.23	14.29	16.83	16.00	16.83	17.36
Zr/Hf	45.71	45.19	44.56	45.75	47.45	46.45	51.26	42.55	44.01	48.74	51.26	49.02	34.39	37.30	41.87	45.36	44.62
Sm–Nd isotopes																	
$^{147}Sm/^{144}Nd$		0.1123		0.1121	0.1119	0.1113	0.1057	0.1376	0.1124				0.1400	0.1168	0.0999		
$^{143}Nd/^{144}Nd$		0.512715		0.512714	0.512704	0.512697	0.512697	0.512721	0.512727				0.512753	0.512722	0.512708		
εNd (185 Ma)		3.50		3.47	3.29	3.17	3.29	3.02	3.73				3.57	3.53	3.64		
2σ		0.14		0.18	0.20	0.16	0.18	0.16	0.18				0.20	0.14	0.14		

See Electronic Appendix 2 for analytical methods

TD Toongi Deposit, *SYN* syenite, *Low Th + U* low-Th + U trachyte, *Med Th + U* medium-Th + U trachyte, *High Th + U* high-Th + U trachyte

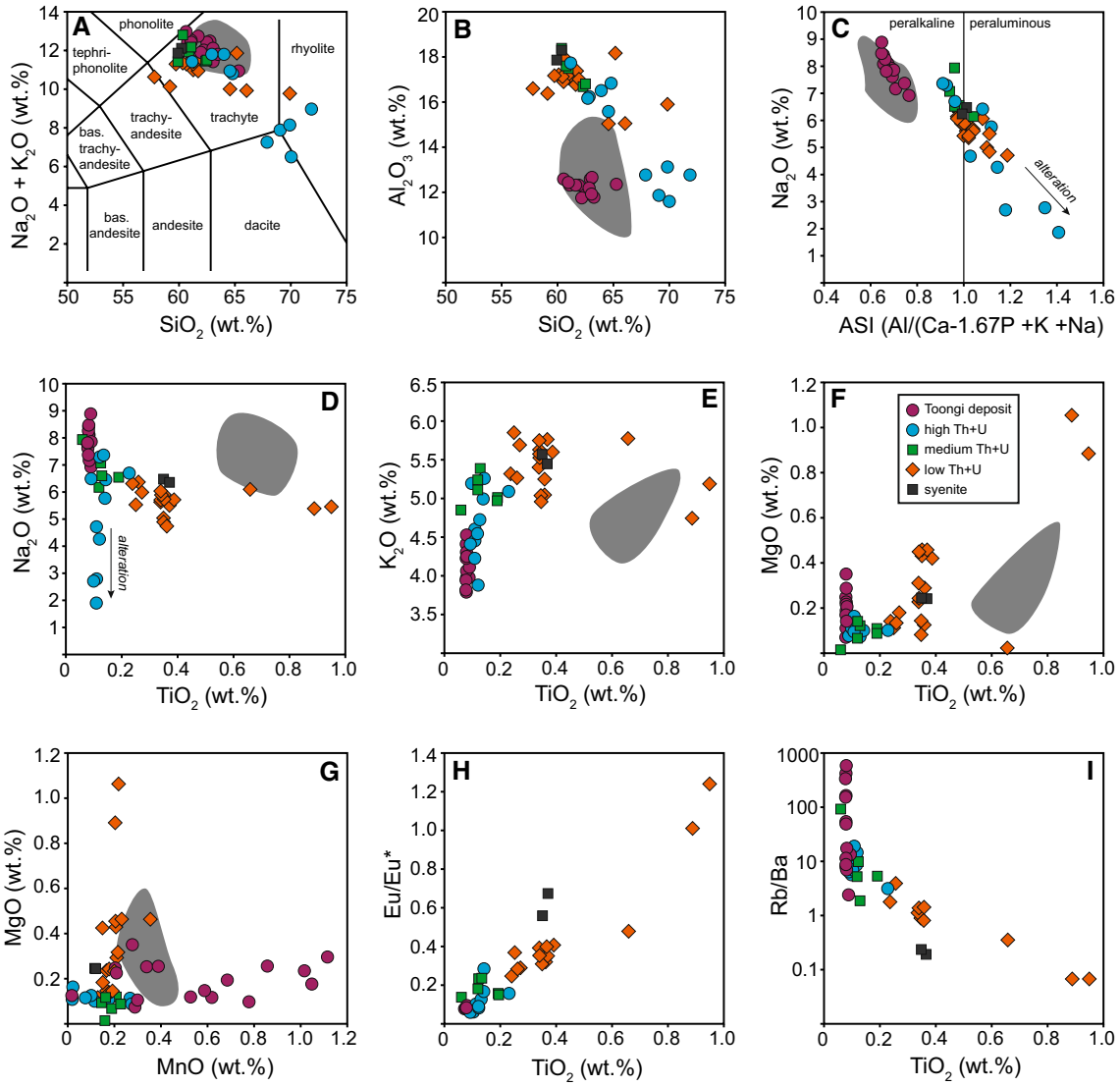

Fig. 7 Scatterplots of the geochemical composition of TAMF igneous rocks. **a** Total alkalis versus SiO_2 (after Le Maitre et al. 2002). **b** Al_2O_3 versus SiO_2. **c** Na_2O versus alumina saturation index (ASI). **d** Na_2O versus TiO_2. **e** K_2O versus TiO_2. **f** MgO versus TiO_2. **g** MgO versus MnO. **h** Eu/Eu* versus TiO_2. **i** Rb/Ba versus TiO_2. The *grey* field represents the composition of pantellerite trachytes from the Menengai and Longonot volcanos, central Kenya (from Macdonald et al. 1970; Rogers et al. 2004; Macdonald et al. 2011)

rock suites, the syenites and low-Th + U trachytes having the lowest ore metal concentrations and the Toongi Deposit trachytes clearly having the highest metal contents. The medium- to high-Th + U trachytes span the range in between, which is consistent with the direct correlation between ore metals and Th and U concentration (Table 3). Ore metal concentrations (represented by Zr in Fig. 9) also positively correlated with most other incompatible trace elements, including Be, Rb, Zn, Ga, Sn, Sb, Cs, Rb/Ba and Pb (Fig. 9e; Table 3), but are negatively correlated with TiO_2 (Fig. 9a). The Nb/Ta ratio of all samples varies between 14 and 18, which are typical values of crustal rocks (e.g. Münker et al. 2003), whereas the Zr/Hf ratio varies from 35 to 55, which is higher than the chondritic value of 34 (Münker et al. 2003). Strontium and Ba concentrations do not vary systematically across the suites, and Cr, Ni, Sc and Co contents are low in all samples. The extensive alteration of some of the high-Th + U trachytes (e.g. Railway prospect) does not significantly affect ore metal grade, except for the light REE (represented by Ce in Fig. 9d), which shows a depletion trend with alteration.

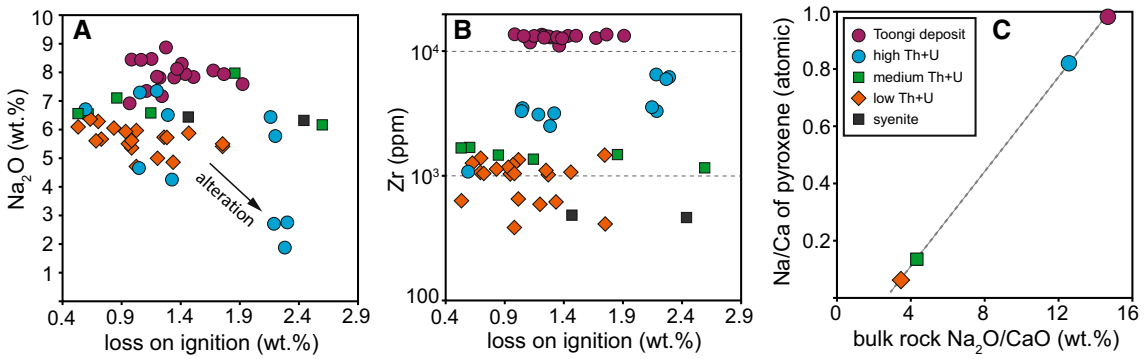

Fig. 8 Scatterplots of the geochemical indicators of alteration for the TAMF igneous rocks. **a** Na_2O versus loss-on-ignition (LOI). **b** Zr versus LOI. **c** Na/Ca of igneous pyroxenes versus bulk-rock Na_2O/CaO

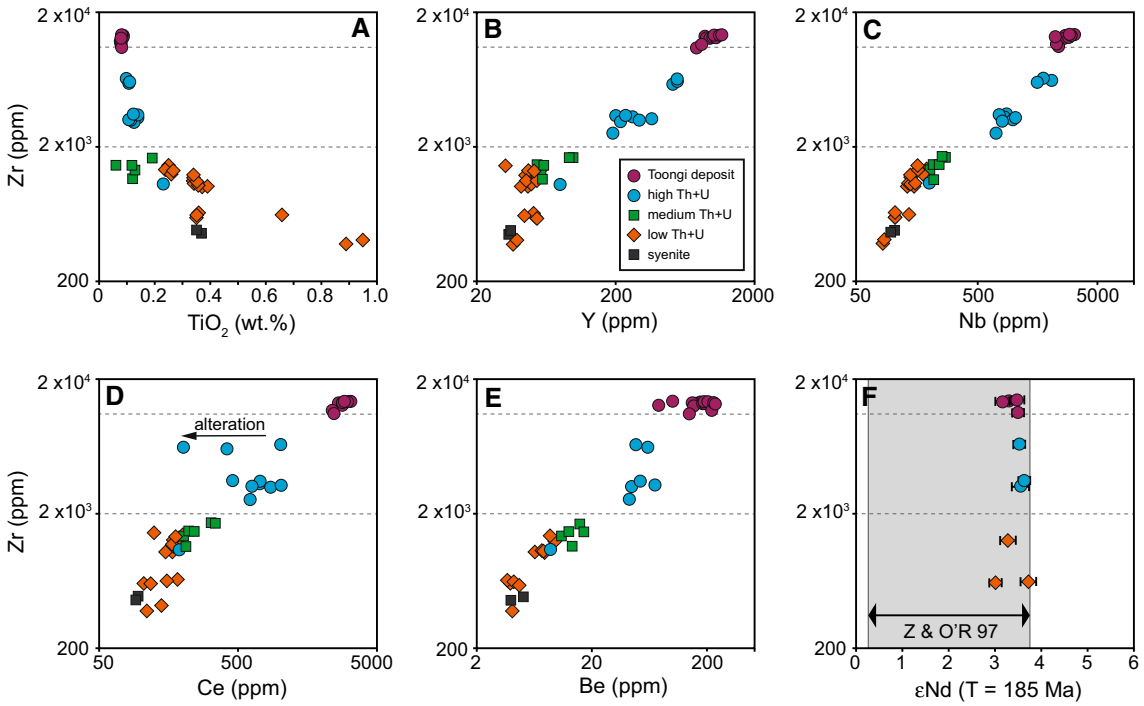

Fig. 9 Scatterplots of ore element geochemistry of TAMF igneous rocks. The plots are Zr versus TiO_2 (**a**), Y (**b**), Nb (**c**), Ce (**d**), Be (**e**) and εNd (**f**). *Note*: the positive correlation between all ore element concentrations, and the similar εNd for all samples. The εNd values are also within the range of εNd values reported for Cenozoic basalts from the Dubbo region by Zhang and O'Reilly (1997) (Z&O'R 97)

Sm–Nd isotope composition

The bulk Sm–Nd isotope composition of a selection of samples from the low-Th + U, high-Th + U and Toongi Deposit trachyte suites were determined to aid evaluation of the source of the magmatic rocks and mineralization. εNd (calculated to the best estimate for formation age of 185 Ma) for all samples fall within a relatively tight range between +3.0 and +3.8. No variation in εNd with ore metal content is observed (Fig. 9f).

Discussion

Origin and evolution of TAMF

Mesozoic plate tectonic reconstructions place the Toongi region to be well inboard of the eastern continental plate margin (Sutherland et al. 2012), so the TAMF likely formed in an intraplate setting associated with the extensive Karoo-Ferrar-SE Australia large igneous province that developed during continental extension related to the break-up

of Pangaea in the early Jurassic (Veevers 2012). Although the TAMF rocks are intermediate in composition, they are associated with basalts (Meakin and Morgan 1999), and they have relatively radiogenic Nd isotope compositions (εNd of +3 to +3.8) that are indicative of derivation from a moderately depleted mantle source.

The boundary between the Lachlan Fold Belt to the south and Gunnedah Basin to the north (Fig. 1a) may represent a crustal-scale structure that allowed mantle-derived magma to traverse the crust towards the surface. Some magma reached the surface with little fractionation to form the basaltic dykes and lava flows of the region. Most of the TAMF, however, consists of relatively evolved intermediate-composition rocks, which requires magma ponding and differentiation prior to eruption or emplacement at, or near, the surface. The relatively uniform and radiogenic Nd isotope compositions (Fig. 9f) rule out a significant role for crustal assimilation in evolution of the TAMF rocks, so we propose that differentiation was achieved via crystal fractionation. The large gravity high that directly underlies the TAMF (Fig. 1b) is interpreted to represent the remnant mafic/ultramafic differentiates of this fractionation process within the crust. Similar gravity anomalies reported beneath other intermediate to felsic alkaline complexes have been interpreted in a similar manner (e.g. Whitaker et al. 2008).

The restricted primary compositional range (from ca. 60 to 66 wt% SiO_2) of the TAMF rocks limits direct geochemical evaluation of the role of crystal fractionation in magma evolution. Nevertheless, modelling of other alkaline magmatic suites have shown that trachytic magma can be produced from a basaltic parental melt via fractionation of olivine, plagioclase, augitic clinopyroxene and Fe–Ti oxides (Baker et al. 1977; Peccerillo et al. 2003; Whitaker et al. 2008; Xu et al. 2010). Therefore, we have undertaken modelling of fractionation of putative parental magmas in an attempt to reproduce the trachyte compositions of the TAMF. We employed the Rhyolite-MELTS algorithm (Gualda et al. 2012) for thermodynamic modelling and used the composition of various Cenozoic mafic lava types from the Dubbo region reported by Zhang and O'Reilly (1997). Despite their difference in ages, these mafic volcanic rocks have similar Nd isotopic signatures to the TAMF (Fig. 9f), suggesting that both of these magma suites derive from a common mantle source. Based on comparison with other intermediate to silicic peralkaline volcanic complexes (see Electronic Appendix 2), we assume a relatively reduced fO_2 condition of 2 log units below the FMQ buffer (FMQ-2), and a starting H_2O content of 0.1 wt% for the modelling (Table 4). Further details of the modelling are outlined in Electronic Appendix 2.

We first attempted to model the formation of the high-K, low-Th + U trachytes that represent the most primitive trachytes of the TAMF (Model 1 in Table 4). The starting parental magma composition used was an olivine tholeiite from Zhang and O'Reilly (1997), as this represents one of the dominant mafic lava types in the region. After extensive iterative testing of model parameters, a reasonable solution was reached by a combination of fractional crystallization (i.e. progressive crystal removal) of the parental melt at 0.3 GPa (to 50% crystallization) followed by equilibrium crystallization (i.e. no crystal removal) of the derivative liquid to a total crystallization of 90% of the parental magma. The fractionating assemblage was olivine, augite, plagioclase, spinel, Fe–Ti oxide and apatite. The resulting melt composition (liquidus at 1025 °C at 0.3 GPa) matches well the composition of the high-K, low-Th + U trachyte, expect for slightly lower Al_2O_3 and Na_2O, and higher K_2O and CaO contents in the modelled melt. These differences are not considered particularly deleterious given the uncertainty in the starting composition and model parameters. Moreover, simple modelling of incompatible trace element (Zr, Nb and Ce) enrichment with fractionation also returns trace element concentration values that are similar to those of the high-K, low-Th + U trachytes (Table 4). The preservation of intermediate-composition feldspar in these rocks indicates that these trachytic melts may have been tapped to the surface with relatively little intervening fractionation at shallower crustal levels (Fig. 10).

Based on the geochemistry trends (Figs. 7, 9) and phenocryst assemblages, we expect that further fractionation of clinopyroxene, alkali feldspar and Fe–Ti oxide drove magma compositions from the high-K, low-Th + U trachytes and syenites to the high-Th + U trachytes that feature relatively low TiO_2, low K_2O and low MgO, but high contents of incompatible elements (Fig. 9). The progressive development of the negative Eu anomalies (Fig. 7h) and increasing Rb/Ba (Fig. 7i) are also consequences of extensive feldspar fractionation. Biotite or muscovite are unlikely to have had any significant role in magmatic fractionation, as they are not found as igneous phases, and all of the analysed samples have typical crustal Nb/Ta of around 15. Igneous rocks that have undergone extensive mica fractionation have low Nb/Ta (<10; Stepanov et al. 2014).

Some samples of the high-Th + U trachytes, such as those from the Railway prospect, deviate from the fractionation trends, have relatively high SiO_2, high LOI and low Na_2O and are variably depleted in LREE (Fig. 9d). Petrographic observations of these samples reveal pervasive low-temperature alteration, including silicification, which likely explains their anomalous geochemical compositions. The mobility of LREE during alteration is consistent with observations from other silicic alkaline volcanic systems (Weaver et al. 1990).

Table 4 Magma fractionation modelling using Rhyolite-MELTS

Fractionation stage	MODEL 1: high-K, low-Th + U trachyte				MODEL 2: Toongi Deposit trachyte				
	1	2	3	4	5	6	7	8	9
Liquidus T at 0.3 GPa (°C)	1252	1135	1025	1062	1285	1015			
Liquidus T at 0.1 GPa (°C)							955	<955	<975
Crystallization mode		Fractional	Equilibrium			Fractional	Equilibrium	Fractional	
% Crystallization of parental melt	0	50	90		0	85	90	93	
wt% oxide									
SiO_2	50.03	48.59	62.51	62.38	45.15	54.84	58.81	60.18	63.02
TiO_2	1.92	3.62	0.48	0.45	2.52	0.62	0.26	0.12	0.08
Al_2O_3	14.87	14.71	15.54	17.33	13.58	12.57	11.05	13.27	12.41
FeO	11.35	14.72	4.95	5.41	12.82	13.7	9.97	5.98	6.54
MnO	0.18	0.34	0.32	0.21	0.20	0.27	0.16	0.18	0.59
MgO	8.21	3.67	0.65	0.31	10.60	0.20	0.02	0.03	0.19
CaO	9.30	7.97	3.40	1.51	10.41	4.21	3.43	3.88	0.42
Na_2O	2.76	3.70	4.57	5.94	3.21	8.12	10.36	10.78	8.14
K_2O	0.95	1.81	6.52	5.4	0.72	4.15	4.46	4.16	4.17
P_2O_5	0.33	0.66	0.10	0.09	0.70	0.66	0.52	0.02	0.01
H_2O/LOI	0.10	0.20	0.95	0.76	0.10	0.66	0.96	1.39	1.38
TRMO*	–	–	–	0.20	–	–	–	–	3.05
Total	100	100	100	100	100	100	100	100	100
Trace element (ppm)									
Zr	140		1120	973	229			2620	13,300
Nb	24		192	150	72			825	2810
Ce	37		259	165	86			860	2870

See Electronic Appendix 2 for modelling details. All calculations at fO_2 conditions of FMQ-2

* TRMO = Total rare metal (Zr, REE, Nb, Y) oxides

Fractionation stages

1. Average of 6 olivine tholeiite analyses from the Dubbo region from Zhang and O'Reilly (1997)
2. Derivative liquid after 50% fractional crystallization of composition 1 at 0.3 GPa
3. Derivative liquid after equilibrium crystallization of composition 2 at 0.3 GPa
4. Average high-K, low-Th + U trachyte from the Toongi Valley and Ugothery units
5. Average of 2 alkali olivine basalt analyses from the Dubbo region from Zhang and O'Reilly (1997)
6. Derivative liquid after 85% fractional crystallization of composition 5 at 0.3 GPa
7. Derivative liquid after equilibrium crystallization of composition 6 at 0.1 GPa
8. Derivative liquid after fractional crystallization of aegirine (2% of total mass), K-feldspar (1%), apatite and Fe–Ti oxide from composition 7 at 0.1 GPa
9. Average Toongi Deposit trachyte

Evolution of the Toongi Deposit trachyte

The Toongi Deposit trachyte is distinct from other trachytes of the TAMF in a number of ways. Not only does the Toongi Deposit trachyte have ore grade concentrations of rare metals, but also has significantly higher concentrations of Na_2O, MnO and incompatible trace elements (e.g. Be, Sn, Th, U) and lower concentrations of K_2O and Al_2O_3 than other trachytes in the region. The Toongi Deposit is distinctly peralkaline (PI = 1.4–1.5), and consists of aegirine, K-feldspar and albite, as opposed to the calcic clinopyroxene and intermediate-composition alkali feldspar of other TAMF trachytes. Most samples of the Toongi Deposit trachyte are altered to varying degrees, which is likely to have affected the composition of these rocks to some extent. However, the fundamental chemical and petrological differences between the magma suites are unlikely due to alteration for several reasons; (1) LOI (a chemical proxy for alteration) does not correlate with distinguishing chemical factors such as Na_2O or Zr content (Fig. 8);

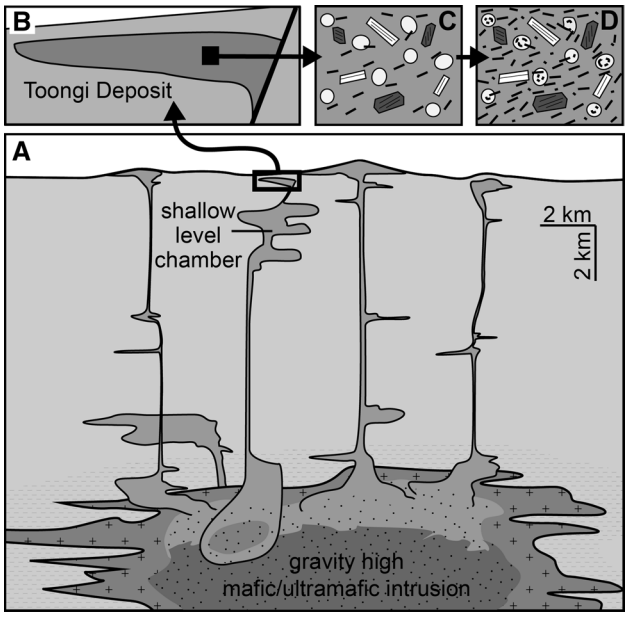

Fig. 10 Schematic upper crustal section of the magmatic evolution of the TAMF. The large mafic/ultramafic intrusion at ca. 10 km depth is inferred from the high-gravity anomaly shown in Fig. 1b. Most TAMF bodies were formed from magma that underwent deep fractionation, whereas the Toongi Deposit trachyte is interpreted to have formed after extensive magma fractionation at shallow crustal levels. The Toongi magma may also have undergone liquid unmixing to form immiscible blebs rich in rare metal, Na silicate liquid (*white* blebs in *panel C*), that subsequently entrained fine crystals of matrix feldspar and aegirine to form snowball EMG (*panel D*)

(2) the Toongi Deposit trachyte is remarkably constant in composition (Fig. 5; Electronic Appendix 2), irrespective of the degree of rock alteration (perhaps with the exception of Sr and Ba) and (3) the high bulk-rock Na_2O is consistent with the highly sodic nature of igneous aegirine from these rocks (Fig. 8c). Therefore, we consider these distinct chemical differences to reflect primary magmatic variations between the rock suites.

The distinct composition of the Toongi Deposit trachyte is unlike most other trachytes worldwide: The closest analogues are the pantellerite trachytes of the Menengai and Longonot volcanoes of central Kenya (Macdonald et al. 1970; Rogers et al. 2004; Macdonald et al. 2011). These volcanic rocks have similar major element composition to the Toongi Deposit trachyte (Fig. 9), except they have significantly higher TiO_2 and lower incompatible trace element contents. The Kenyan trachytes are also mineralogically distinct, having phenocrysts of alkali feldspar, fayalite, Fe–Ti oxide and (in some cases) aenigmatite, rather than two feldspars and aegirine.

The Toongi Deposit trachyte and other TAMF trachytes have close spatial and temporal associations and have similar Nd isotope compositions, and so are likely to have some direct genetic relationship. We can discount a significant role for crustal assimilation based on the similar Nd isotope results of all suites, and we do not expect that variable H_2O contents affected different evolutionary paths of these magma suites, as there are no primary hydrous phases in the Toongi Deposit trachyte, and there is no chemical evidence of fractionation of hydrous phases, such as micas (e.g. fractionated Nb/Ta; Stepanov et al. 2014).

Extensive Rhyolite-MELTS testing of fractionation of the olivine tholeiite parent magma composition used for modelling of the high-K, low-Th + U trachytes (see above) using a range of parameters (fO_2, P, T) failed to produce liquids of comparable composition to the Toongi Deposit trachyte. This result indicates that the parental magma to the Toongi Deposit trachyte may be distinct from that of other rocks of the TAMF. Therefore, subsequent modelling employed an alkali olivine basalt composition (see Model 2 in Table 4) that also occurs in the Dubbo region (Zhang and O'Reilly 1997). In this case, we also assumed a fO_2 value of FMQ-2 and initial H_2O content of 0.1 wt%. Again, we conducted iterative testing of model parameters and found a reasonable solution by a combination of fractional crystallization of the parental melt at 0.3 GPa to 85% of the starting mass, followed by equilibrium crystallization of the derivative liquid at 0.1 GPa to a total crystallization of 90% of the parental magma. The fractionating assemblage was again olivine, augite, plagioclase, Fe–Ti spinel and apatite, but in this case the combination of a different parental melt, more extensive degree of fractional crystallization and polybaric evolution produced an intermediate melt composition with the low Al_2O_3, high FeO and high Na_2O/K_2O that is characteristic of the Toongi Deposit trachyte. Based on the natural phenocrysts assemblage, we further removed components of aegirine (2%), K-feldspar (1%), and trace apatite and Fe–Ti oxide to produce an even better model fit to the natural composition (Table 4). The only significant mismatch between the model and observed compositions is the higher CaO and Na_2O in the modelled melt. A simple incompatible element enrichment model after 93% total crystallization of the parental magma also fails to reproduce the very high levels of incompatible trace elements in the Toongi Deposit trachyte.

Our model of extensive polybaric fractionation of alkali olivine basalt can broadly reproduce the melt composition of the Toongi Deposit trachyte and, hence, may also be applicable to other pantellerite trachyte magmas such as at Menengai and Longonot, Kenya. Nonetheless, the low TiO_2 and CaO, high incompatible trace element contents, and abundance of aegirine and two feldspars in the Toongi Deposit trachyte requires further explanation. These features can be reconciled if the magma underwent extensive further fractionation at low pressures and down to low temperatures (<700 °C), although modelling with Rhyolite-MELTS produced progressively SiO_2-enriched melts with

further fractionation. We suspect that the Rhyolite-MELTS algorithm may not be well suited to these relatively extreme magmatic conditions, as, for example, aegirine saturation is not reached. Instead, we speculate that further magmatic differentiation was driven by extensive aegirine plus feldspar fractionation, perhaps at, or approaching, eutectic-like conditions. Extensive feldspar fractionation is evident from the pronounced negative Eu anomalies (Fig. 7h) and very high Rb/Ba (Fig. 7i). Crystallization down to low temperatures may have been facilitated by the high incompatible element and F contents (Manning 1981), and it provides an explanation for the two-feldspar mineral assemblage. The high peralkalinity and high Na_2O/CaO composition should favour fractionation of aegirine over Fe oxides or fayalite as the dominated Fe-bearing phase (Marks et al. 2011). The absence of aenigmatite is likely due to the low TiO_2 and relatively low SiO_2 contents (Macdonald et al. 2011) and the lack of arfvedsonite is interpreted to be due to the low activity of H_2O in the magma. Marks et al. (2011) show that aegirine crystallization is favoured in melts with high activity of Na_2O over a large range of intrinsic oxygen fugacity, but extended aegirine fractionation will lead to Fe^{3+} depleted—and hence even more reduced—melt compositions (Markl et al. 2010). The lack of fractionation of a divalent cation-dominant phase also explains the relatively high MnO and, to some extent, MgO contents of the Toongi Deposit trachyte (Fig. 7g), as under these conditions these elements are highly incompatible, and hence are enriched in the residual melt with the progress of fractionation. The dark Mn-rich patches dispersed throughout the rock are interpreted to be late-stage precipitates of Mn oxide and silicates from trapped pockets of highly fractionated residual melt.

Origin of the rare metal mineralization

The ore of the Toongi Deposit is remarkably uniform in grade (Fig. 5) and distribution and is entirely contained within the trachyte body with no mineralization halo in the surrounding country rocks. These characteristics are consistent with a direct igneous association to mineralization, as has been recognized globally for rare metal mineralization in peralkaline igneous rocks (Chakhmouradian and Zaitsev 2012). Our magma evolution modelling results (Table 4), together with systematic trends in incompatible element geochemistry and a common Nd isotope signature for igneous rocks across the TAMF (Fig. 9f), all lend support to a model whereby ore element concentrations of the Toongi Deposit were obtained—for the most part—through extensive crystal fractionation prior to magma emplacement at shallow crustal levels. Crystallization likely proceeded to low temperatures, but the trachytic texture of the rock indicates a late stage of rapid cooling, so textural evidence of an igneous origin for mineralization may well be preserved in these rocks. Thus, we now discuss ore mineral paragenesis based on textural associations and mineral chemistry.

Primary ore mineral assemblage

The dominant ore mineral is the Na–Zr–silicate phase, tentatively identified as an EGM, that forms the snowball-textured blebs disseminated through the matrix of the Toongi Deposit trachyte. Simple mass balance budgeting based on mineral and bulk-rock composition and mineral proportions (e.g. Fig. 6a) indicate that this phase, together with lueshite/natroniobite, host the vast majority (>80%) of ore metals in the deposit. Both the EGM and lueshite/natroniobite are dispersed throughout the rock matrix, but appear in textural equilibrium with igneous aegirine and feldspar. The snowball EGM is interstitial to igneous phenocrysts and matrix minerals, but also include matrix feldspar and aegirine crystals of igneous origin; we therefore assign the EGM to be a late magmatic phase. The co-crystallization of EGM and the Mn oxides (Fig. 4f, g) in the Mn-rich patches also conforms to a late magmatic origin. Further discussion on the origin and significance of the snowball texture of this phase is presented further below.

Lueshite/natroniobite is also seen filling interstices between igneous phases in the rock matrix (Fig. 4h) indicating it formed at a similar stage of magmatic evolution as the EGM. Vlasovite and catapleiite are also likely to be of late magmatic origin, as they have similar textural settings to the EGM. These phases are relatively minor compared to the EGM, and the reason for their formation instead of EGM is unclear, but may relate to localized variations in Na/Ca or Si/Zr in the interstitial residual melt fraction.

Secondary ore mineral assemblage

Filling micro-fractures and vesicles in the trachyte is a secondary ore mineral assemblage of REE (fluoro)carbonates, yttrian milarite and hydrated Na–Ca–Zr silicates, such as catapleiite and gaidonnayite. The fractures are irregular and discordant to the trachytic flow foliation, and ore minerals occur with alteration minerals such as sericite and chlorite that have reaction relationships with igneous minerals (Fig. 4i). Ore minerals in the fractures tend to occur as irregular fine-grained aggregates, whereas the vesicle fill occurs as fine colloidal banding, or euhedral prismatic crystals that are typical of growth into open cavities. In both cases, these ore minerals are interpreted to have formed via late- or post-magmatic hydrothermal alteration. The prevalence of fractionated Y/Ho and the tetrad effect on the REE geochemistry of these phases (Fig. 7b) is also consistent with a hydrothermal origin (Bau 1996; Schmitt et al. 2002; Monecke et al. 2011). Based on the composition of the ore

mineral assemblage, we suggest that fluids for this alteration were Ca- and Sr-bearing CO_2–H_2O fluids that were derived either as hydrothermal fluids exsolved from the crystallizing and cooling laccolith or from localized devolatilization of the Grega Group country rock due to intrusion of the Toongi trachyte. The latter case would be akin to the processes responsible for endoskarn formation (Meinert 1992). Alteration of the cooling trachyte by these fluids led to localized dissolution of some of the primary ore minerals and redistribution into vesicles and micro-fractures in the rock. This metal redistribution process led to a greater degree of heterogeneity in ore metal distribution between phases (Fig. 6b), but does not appear to have modified ore metal grades at the hand sample scale (Fig. 5), indicating that hydrothermal ore metal remobilization was likely limited to the sub-metre (probably cm) scale. The lack of extensive alteration of the country rock around the deposit (e.g. lack of fenitization) also supports a limited role for hydrothermal activity, as other mineralized intrusions that have undergone extensive hydrothermal alteration and ore remobilization do feature an extensive zone of metasomatic alteration extending around the outer margins of the intrusion (e.g. Dostal et al. 2014).

Role of magmatic processes in ore formation

Based on the geochemical and textural data it appears that most, if not all, of the ore metals were concentrated in the deposit under magmatic conditions. Na–Zr–silicates and Na–Nb oxide of igneous origin have been reported from many alkaline igneous bodies (e.g. Chakhmouradian and Mitchell 1998; Marks et al. 2011) and are consistent with expected phase relations for high-Na_2O, low-CaO, peralkaline magmas that crystallize aegirine (Marks et al. 2011), such as Toongi Deposit trachyte. Globally, peralkaline igneous rocks of this association are relatively rare, but they often host significant Zr–Nb–REE mineralization because these elements have high solubilities in sodic peralkaline melts, allowing for high concentrations in residual melts formed after extensive fractional crystallization. If these melts have low initial H_2O contents and low fO_2 (e.g. Markl et al. 2010)—as we expect for the Toongi magma—then H_2O activity in the melt will remain low, and volatile saturation, if reached, will likely release CH_4-dominated fluids (Markl et al. 2010). These fluids are unlikely to sequester halogens (Cl, F), alkaline elements (K, Na) or rare metals (Zr, Nb, REE), meaning the concentration of these elements in the melt will continue to increase with fractionation. Elevated F content of the melt may have an additional effect of increasing rare metal solubility in the residual melt (Aseri et al. 2015). Even if H_2O-rich fluids had exsolved from the crystallizing magmatic body, the volume of this fluid would be relatively small and its capacity to remove alkali elements and rare metals would be limited. Evidence that these derivative melts can obtain very high rare metal contents come from studies of melt inclusions from peralkaline complexes (Kovalenko et al. 1995; Schmitt et al. 2002), which have rare metal contents as high as, or higher than, the ore grades at Toongi. Therefore, key features that distinguish the Toongi Deposit trachyte from other TAMF trachytes, such as the peralkaline composition and extreme degree of fractionation, were also critically important for producing the ore grade mineralization that is unique to the Toongi Deposit.

The possible role of liquid immiscibility

A distinctive feature of the Toongi ore is the globular or snowball texture of the Na–Zr–silicates (Fig. 4) and their near uniform distribution throughout the trachyte. The snowball-textured grains resemble snowball quartz described from peralkaline granites (Schwartz 1992; Helba et al. 1997; Müller et al. 2000), although the Na–Zr–silicate snowball grains rarely take on euhedral forms and their mineral inclusions tend to form swirl and spiral patterns within the grains, rather than aligning with growth zones of the host mineral, or aligning with the flow banding of the rock matrix. The snowball Na–Zr–silicates are also commonly protruded by feldspar or aegirine phenocrysts and, in Mn-rich zones, feature Mn oxides crystals that grew from the outer margin of the snowball in towards the interior of the grain (Fig. 4g). Collectively, these features indicate that the snowball Na–Zr–silicates precipitated from a liquid phase that was present within the rock during formation of the igneous matrix minerals, but this liquid was a separate phase to that which crystallized the matrix minerals. We suggest that the clusters of matrix minerals included in the snowball Na–Zr–silicates were entrained into the liquid, rather than crystallized from it. If this is the case, it would imply that there were two immiscible liquids present in the rock: one aluminosilicate melt that crystallized the feldspar and aegirine, and one Na–Zr silicate liquid that crystallized the bulk of the ore minerals of the Toongi Deposit (see Fig. 10). This premise is consistent with the general globular texture of the EGM blebs in the rock, which resemble liquid immiscibility textures (e.g. Philpotts 1978; Kjarsgaard and Hamilton 1988) and may help to explain the very high concentration of ore metals throughout the trachyte body. Direct precipitation EGM from blebs of an immiscible liquid that was enriched in incompatible elements would not only explain the snowball texture and the homogeneous distribution of these phases, but would also help reconcile the unusual incompatible-element-rich bulk composition of this phase.

Our premise for liquid immiscibility during ore formation is based primarily on textural interpretation and, as

such, is tentative. Nevertheless, there is growing evidence that silicate liquid immiscibility can have an important role in forming rare metal mineralization in igneous environments. Liquid immiscibility is favoured in peralkaline melt compositions (Veksler 2004), and experimental studies have demonstrated that Zr and other rare metals are soluble to high concentrations in Al-deficient, Na silicate liquids (Smirnov et al. 2012; Louvel et al. 2013). Evidence of liquid immiscibility has been reported in many rare metal-rich alkaline complexes (Markl 2001; Sørensen et al. 2003; Rajesh 2003; Petrella et al. 2014; Vasyukova and Williams-Jones 2014), of which the most relevant here is the work of Markl (2001) and Petrella et al. (2014) who propose that Zr, Nb and REE have strong affinities with Al-poor silicate liquids, a premise consistent with our observations for Toongi. If silicate liquid unmixing did occur during low-pressure fractionation of the Toongi trachyte, then separation and concentration of the metal-rich liquid fraction into the laccolith structure that now represents the Toongi Deposit trachyte (Fig. 10) may have been an important process in producing the high metal grades in the Toongi Deposit.

Comparison to other rare metal-rich alkaline complexes

A large fraction of the world's rare metal ore resources is hosted by peralkaline intrusive complexes, such as the Strange Lake and the Thor Lake intrusions of Canada (Boily and Williams-Jones 1994; Sheard et al. 2012), the Bokan Mountain Complex, Alaska (Dostal et al. 2014), and the Tamazeght intrusion of Morocco (Salvi et al. 2000). Mineralization in these intrusions is thought to result primarily from magmatic processes related to extensive fractional crystallization of peralkaline magma (Chakhmouradian and Zaitsev 2012), a model that we also propose for the Toongi Deposit. In many respects, Toongi and the Strange Lake Pluton share many features, including similar ore grades and ore mineralogy (Salvi and Williams-Jones 1995; Gysi and Williams-Jones 2013), and a magmatic ore genesis model involving extensive crystal fractionation under conditions of low magmatic fO_2 and H_2O activity (Boily and Williams-Jones 1994), with a possible role for liquid immiscibility (Vasyukova and Williams-Jones 2014), and late-stage hydrothermal remobilization of ore metals by influx of external Ca-bearing fluids (Salvi and Williams-Jones 1995, 1996). Late-stage hydrothermal remobilization of primary rare metal minerals by Ca- and/or C–O–H-rich fluids has also been reported from other intrusive complexes (e.g. Salvi et al. 2000; Schmitt et al. 2002; Kynicky et al. 2011; Sheard et al. 2012) and may be common feature of rare metal mineralization in alkaline complexes in general (see also Salvi and Williams-Jones 2006).

The most distinct difference between Toongi and rare metal-rich plutonic complexes relates to the environment and conditions of magma emplacement. The slow cooling of rare metal-rich plutons have the potential to eradicate primary mineralization textures via subsolidus re-equilibration and/or alteration during cooling, which complicates textural interpretation of these rocks. By contrast, Toongi was emplaced at very shallow depths, which allowed rapid cooling to form the trachytic textures of the rock. Therefore, the primary magmatic textures and mineral compositions in the Toongi Deposit are well preserved, which greatly aids in understanding ore genesis processes. In particular, the textural evidence of liquid immiscibility at Toongi would be unlikely to be preserved in slow cooled plutonic environments. In this case, the textural preservation at Toongi may also be beneficial for understanding magmatic processes of rare metal mineralization more broadly.

As far as we are aware, the only other volcanic-hosted rare metal deposit of significance is the Brockman deposit of Western Australia (Ramsden et al. 1993; Taylor et al. 1995). The Brockman deposit is similar to Toongi in that mineralization consists of unusual Zr silicates (so-called "zircon gel"; Ramsden et al. 1993) niobate minerals and REE carbonates, and is hosted in peralkaline rocks of trachyte to rhyolite composition. Taylor et al. (1995) suggest that the volcanic rocks and associated mineralization at Brockman evolved via extensive crystal fractionation with some assimilation of crustal rocks. However, Brockman differs from Toongi in that the Brockman ore is very fine grained (<20 μm) and was probably extensively remobilized by F-rich hydrothermal fluids, which now manifests as abundant fluorite in association with the ore horizon, and extensive zones of Na depletion in the volcanic sequence (Ramsden et al. 1993; Taylor et al. 1995).

Conclusions

The Toongi Deposit is an exceptional example of rare metal mineralization hosted in trachyte emplaced close to the Earth's surface. Rare metal concentrations reached ore grades primarily through extensive fractionation of mantle-derived alkaline magma at shallow crustal levels, under low-fO_2- and low-H_2O-activity conditions. There is evidence that the magma underwent unmixing to produce an immiscible rare metal-rich Na silicate liquid at the latest stages of fractionation, with this immiscible liquid forming most of the ore minerals of the deposit. Subsequent hydrothermal alteration of the ore was limited to localized remobilization of ore metals into micro-fractures and vesicles within the rock. The excellent preservation of primary ore textures and minerals at Toongi provides a unique

opportunity to study rare metal mineralization processes in alkaline magmatic systems and hence may be applicable to other rare metal deposits, including those hosted in plutonic rocks where primary ore textures and minerals may have been modified during slow cooling.

Acknowledgements This work was supported by an ARC Future Fellowship (FT 120100198) to Spandler. We thank Terry Ransteed and Ian Chalmers from Alkane Resource Ltd. for providing field support and access to drillcore samples and assay data, and Kevin Blake (JCU) for assistance with the electron microprobe analysis. Comments from two reviewers and editor in chief Othmar Müntener contributed to a much-improved manuscript.

References

Alkane Resources Limited (2015) Annual report. http://www.alkane.com.au/index.php/reports/annual-reports

Aseri AA, Linnen RL, Che XD, Thibault Y, Holtz F (2015) Effects of fluorine on the solubilities of Nb, Ta, Zr and Hf minerals in highly fluxed water-saturated haplogranitic melts. Ore Geol Rev 64:736–746

Aubert D, Stille P, Probst A, Gauthier-Lafaye F, Pourcelot L (2002) Characterization and migration of atmospheric REE in soils and surface waters. Geochim Cosmochim Acta 66:3339–3350

Baker BH, Goles GG, Leeman WP, Lindstrom MM (1977) Geochemistry and petrogenesis of a basalt-benmoreite-trachyte suite from the southern part of the Gregory Rift, Kenya. Contrib Mineral Petrol 64:303–332

Bau M (1996) Controls on the fractionation of isovalent trace elements in magmatic and aqueous systems: evidence from Y/Ho, Zr/Hf, and lanthanide tetrad effect. Contrib Mineral Petrol 123:323–333

Boily M, Williams-Jones AE (1994) The role of magmatic and hydrothermal processes in the chemical evolution of the Strange Lake plutonic complex, Quebec-Labrador. Contrib Mineral Petrol 118:33–47

Chakhmouradian AR, Mitchell RH (1998) Lueshite, pyrochlore and monazite-(Ce) from apatite-dolomite carbonatite, Lesnaya Varaka complex, Kola Peninsula, Russia. Mineral Mag 62:769–782

Chakhmouradian AR, Wall F (2012) Rare earth elements: minerals, mines, magnets (and more). Elements 8:333–340

Chakhmouradian AR, Zaitsev AN (2012) Rare earth mineralization in igneous rocks: sources and processes. Elements 8:347–353

Dostal J (2016) Rare metal deposits associated with alkaline/peralkaline igneous rocks. In: Verplank PL, Hitzman MW (eds) Rare earth and critical elements in ore deposits. Reviews in Economic Geology vol 18. Society of Economic Geologists, Littleton, CO, pp 33–54

Dostal J, Kontak DJ, Karl SM (2014) The early Jurassic Bokan Mountain peralkaline granitic complex (southeastern Alaska): geochemistry, petrogenesis and rare-metal mineralization. Lithos 202:395–412

Duggan MB (1990) Wilkinsonite, $Na_2Fe_4^{2+}Fe_2^{3+}Si_6O_{20}$, a new member of the aenigmatite group from the Warrumbungle Volcano, New South Wales, Australia. Am Mineral 75:694–701

Dulhunty JA (1967) Mesozoic alkaline volcanism and Garrawilla Lavas near Mullaley, New South Wales. J Geol Soc Aust 14:133–138

Elderfield H, Greaves MJ (1982) The rare earth elements in seawater. Nature 296:214–219

Foster DA, Gray DR (2000) Evolution and structure of the Lachlan Fold Belt (Orogen) of eastern Australia. Ann Rev Earth Planet Sci 28:47–80

Frost BR, Barnes CG, Collins WJ, Arculus RJ, Ellis DJ, Frost CD (2001) A geochemical classification for granitic rocks. J Petrology 42(11):2033–2048

Gualda GA, Ghiorso MS, Lemons RV, Carley TL (2012) Rhyolite-MELTS: a modified calibration of MELTS optimized for silica-rich, fluid-bearing magmatic systems. J Petrol 53:875–890

Gysi AP, Williams-Jones AE (2013) Hydrothermal mobilization of pegmatite-hosted REE and Zr at Strange Lake, Canada: a reaction path model. Geochim Cosmochim Acta 122:324–352

Harrison TM, Blichert-Toft J, Müller W, Albarede F, Holden P, Mojzsis SJ (2005) Heterogeneous Hadean hafnium: evidence of continental crust at 4.4 to 4.5 Ga. Science 310:1947–1950

Hawthorne FC, Abdu YA, Ball NA, Černý P, Kristiansen R (2014) Agakhanovite-(Y), ideally (YCa) $_2KBe_3Si_{12}O_{30}$, a new milarite-group mineral from the Heftetjern pegmatite, Tørdal, Southern Norway: description and crystal structure. Am Mineral 99:2084–2088

Helba H, Trumbull RB, Morteani G, Khalil SO, Arslan A (1997) Geochemical and petrographic studies of Ta mineralization in the Nuweibi albite granite complex, Eastern Desert, Egypt. Miner Depos 32:164–179

Hofmann AW (1997) Mantle geochemistry: the message from oceanic volcanism. Nature 385:219–229

Horbe AMC, da Costa ML (1999) Geochemical evolution of a lateritic Sn–Zr–Th–Nb–Y–REE-bearing ore body derived from apogranite: the case of Pitinga, Amazonas—Brazil. J Geochem Explor 66:339–351

Kjarsgaard BA, Hamilton DL (1988) Liquid immiscibility and the origin of alkali-poor carbonatites. Mineral Mag 52:43–55

Kovalenko VI, Tsaryeva GM, Goreglyad AV, Yarmolyuk VV, Troitsky VA, Hervig RL, Farmer G (1995) The peralkaline granite-related Khaldzan-Buregtey rare metal (Zr, Nb, REE) deposit, western Mongolia. Econ Geol 90:530–547

Kynicky J, Chakhmouradian AR, Xu C, Krmicek L, Galiova M (2011) Distribution and evolution of zirconium mineralization in peralkaline granites and associated pegmatites of the Khan Bogd complex, southern Mongolia. Can Mineral 49:947–965

Le Maitre RW, Streckeisen A, Zanettin B, Le Bas MJ, Bonin B, Bateman P et al (2002) Igneous rocks. A classification and glossary of terms. Recommendations of the IUGS Subcomission on the Systematics of Igneous Rocks, Cambridge Univ Press, Cambridge, p 236

Louvel M, Sanchez-Valle C, Malfait WJ, Testemale D, Hazemann JL (2013) Zr complexation in high pressure fluids and silicate melts and implications for the mobilization of HFSE in subduction zones. Geochim Cosmochim Acta 104:281–299

Macdonald R, Bailey DK, Sutherland DS (1970) Oversaturated peralkaline glassy trachytes from Kenya. J Petrol 11:507–517

Macdonald R, Bagiński B, Leat PT, White JC, Dzierżanowski P (2011) Mineral stability in peralkaline silicic rocks: information from trachytes of the Menengai volcano, Kenya. Lithos 125:553–568

Manning DAC (1981) The effect of fluorine on liquidus phase relationships in the system Qz–Ab–Or with excess water at 1 kb. Contrib Mineral Petrol 76:206–215

Markl G (2001) A new type of silicate liquid immiscibility in peralkaline nepheline syenites (lujavrites) of the Ilimaussaq complex, South Greenland. Contrib Mineral Petrol 141:458–472

Markl G, Marks MA, Frost BR (2010) On the controls of oxygen fugacity in the generation and crystallization of peralkaline melts. J Petrol 51:1831–1847

Marks MA, Hettmann K, Schilling J, Frost BR, Markl G (2011) The mineralogical diversity of alkaline igneous rocks: critical factors for the transition from miaskitic to agpaitic phase assemblages. J Petrol 52:439–455

McDougall I (2008) Geochronology and the evolution of Australia in the Mesozoic. Aust J Earth Sci 55:849–864

Meakin NS, Morgan EJ (1999) Dubbo 1:250,000 geological sheet SI/55-4, 2nd edn. Explanatory Notes. Geol Surv New South Wales, Sydney

Meinert LD (1992) Skarns and skarn deposits. Geosci Can 19(4):145–162

Monecke T, Kempe U, Trinkler M, Thomas R, Dulski P, Wagner T (2011) Unusual rare earth element fractionation in a tin-bearing magmatic-hydrothermal system. Geology 39:295–298

Müller A, Seltmann R, Behr HJ (2000) Application of cathodoluminescence to magmatic quartz in a tin granite—case study from the Schellerhau Granite Complex, Eastern Erzgebirge, Germany. Miner Depos 35:169–189

Münker C, Pfänder JA, Weyer S, Büchl A, Kleine T, Mezger K (2003) Evolution of planetary cores and the Earth-Moon system from Nb/Ta systematics. Science 301:84–87

Peccerillo A, Barberio MR, Yirgu G, Ayalew D, Barbieri MW, Wu TW (2003) Relationships between mafic and peralkaline silicic magmatism in continental rift settings: a petrological, geochemical and isotopic study of the Gedemsa volcano, central Ethiopian rift. J Petrol 44:2003–2032

Petrella L, Williams-Jones AE, Goutier J, Walsh J (2014) The nature and origin of the rare earth element mineralization in the Misery syenitic intrusion, northern Quebec, Canada. Econ Geol 109:1643–1666

Philpotts AR (1978) Textural evidence for liquid immiscibility in tholeiites. Mineral Mag 42:417–425

Rajesh HM (2003) Outcrop-scale silicate liquid immiscibility from an alkali syenite (A-type granitoid)-pyroxenite association near Puttetti, Trivandrum Block, South India. Contrib Mineral Petrol 145:612–627

Ramsden AR (1992) Mineralogy of the Toongi rare metal and rare earth prospect, Dubbo, New South Wales: electron microprobe analysis of samples from drill hole TOD-2. Restricted Report 359R, CSIRO Division of Exploration Geoscience

Ramsden AR, French DH, Chalmers DI (1993) Volcanic-hosted rare-metals deposit at Brockman, Western Australia. Miner Depos 28:1–12

Rogers NW, Evans PJ, Blake S, Scott SC, Hawkesworth CJ (2004) Rates and timescales of fractional crystallization from ^{238}U–^{230}Th–^{226}Ra disequilibria in trachyte lavas from Longonot volcano, Kenya. J Petrol 45:1747–1776

Rudnick RL, Gao SX (2003) Composition of the continental crust. Treatise Geochem 3:1–64

Salvi S, Williams-Jones AE (1995) Zirconosilicate phase relations in the Strange Lake (Lac Brisson) pluton, Quebec-Labrador, Canada. Am Mineral 80:1031–1040

Salvi S, Williams-Jones AE (1996) The role of hydrothermal processes in concentrating high-field strength elements in the Strange Lake peralkaline complex, northeastern Canada. Geochim Cosmochim Acta 60:1917–1932

Salvi S, Williams-Jones AE (2006) Alteration, HFSE mineralisation and hydrocarbon formation in peralkaline igneous systems: insights from the Strange Lake Pluton, Canada. Lithos 91:19–34

Salvi S, Fontan F, Monchoux P, Williams-Jones AE, Moine B (2000) Hydrothermal mobilization of high field strength elements in alkaline igneous systems: evidence from the Tamazeght Complex (Morocco). Econ Geol 95:559–576

Schilling J, Wu FY, McCammon C, Wenzel T, Marks MAW, Pfaff K et al (2011) The compositional variability of eudialyte-group minerals. Mineral Mag 75:87–115

Schmitt AK, Trumbull RB, Dulski P, Emmermann R (2002) Zr–Nb–REE mineralization in peralkaline granites from the Amis Complex, Brandberg (Namibia): evidence for magmatic pre-enrichment from melt inclusions. Econ Geol 97:399–413

Schwartz MO (1992) Geochemical criteria for distinguishing magmatic and metasomatic albite-enrichment in granitoids: examples from the Ta–Li granite Yichun (China) and the Sn–W deposit Tikus (Indonesia). Miner Depos 27:101–108

Sheard ER, Williams-Jones AE, Heiligmann M, Pederson C, Trueman DL (2012) Controls on the concentration of zirconium, niobium, and the rare earth elements in the Thor Lake rare metal deposit, Northwest Territories, Canada. Econ Geol 107:81–104

Smirnov SZ, Thomas VG, Kamenetsky VS, Kozmenko OA, Large RR (2012) Hydrosilicate liquids in the system Na_2O–SiO_2–H_2O with NaF, NaCl and Ta: evaluation of their role in ore and mineral formation at high T and P. Petrology 20:271–285

Sørensen H, Bailey JC, Kogarko LN, Rose-Hansen J, Karup-Møller S (2003) Spheroidal structures in arfvedsonite lujavrite, Ilímaussaq alkaline complex, South Greenland: an example of macro-scale liquid immiscibility. Lithos 70:1–20

Stepanov A, Mavrogenes JA, Meffre S, Davidson P (2014) The key role of mica during igneous concentration of tantalum. Contrib Mineral Petrol 167:1–8

Sutherland FL, Graham IT, Meffre S, Zwingmann H, Pogson RE (2012) Passive-margin prolonged volcanism, East Australian Plate: outbursts, progressions, plate controls and suggested causes. Aust J Earth Sci 59:983–1005

Taylor SR, McLennan SM (1985) The continental crust: its composition and evolution. Blackwell Scientific Publications, Hoboken

Taylor WR, Esslemont G, Sun SS (1995) Geology of the volcanic-hosted Brockman rare-metals deposit, Halls Creek Mobile Zone, northwest Australia. II. Geochemistry and petrogenesis of the Brockman volcanics. Mineral Petrol 52:231–255

Thomas R, Webster JD, Rhede D, Seifert W, Rickers K, Förster HJ et al (2006) The transition from peraluminous to peralkaline granitic melts: evidence from melt inclusions and accessory minerals. Lithos 91:137–149

Totterdell JM, Moloney J, Korsch RJ, Krassay AA (2009) Sequence stratigraphy of the Bowen–Gunnedah and Surat Basins in New South Wales. Aust J Earth Sci 56:433–459

Vasyukova O, Williams-Jones AE (2014) Fluoride–silicate melt immiscibility and its role in REE ore formation: evidence from the Strange Lake rare metal deposit, Québec-Labrador, Canada. Geochim Cosmochim Acta 139:110–130

Veevers JJ (2012) Reconstructions before rifting and drifting reveal the geological connections between Antarctica and its conjugates in Gondwanaland. Earth Sci Rev 111:249–318

Veksler IV (2004) Liquid immiscibility and its role at the magmatic–hydrothermal transition: a summary of experimental studies. Chem Geol 210:7–31

Wang Q, Deng J, Liu H, Yang L, Wan L, Zhang R (2010) Fractal models for ore reserve estimation. Ore Geol Rev 37:2–14

Weaver SD, Gibson IL, Houghton BF, Wilson CJN (1990) Mobility of rare earth and other elements during crystallization of peralkaline silicic lavas. J Volcanol Geotherm Res 43:57–70

Weng Z, Jowitt SM, Mudd GM, Haque N (2015) A detailed assessment of global rare earth element resources: opportunities and challenges. Econ Geol 110:1925–1952

Whitaker ML, Nekvasil H, Lindsley DH, McCurry M (2008) Can crystallization of olivine tholeiite give rise to potassic rhyolites? An experimental investigation. Bull Volcanol 70:417–434

Williams-Jones AE, Migdisov AA, Samson IM (2012) Hydrothermal mobilisation of the rare earth elements: a tale of "ceria" and "yttria". Elements 8:355–360

Xu YG, Chung SL, Shao H, He B (2010) Silicic magmas from the Emeishan large igneous province, Southwest China: petrogenesis and their link with the end-Guadalupian biological crisis. Lithos 119:47–60

Zhang M, O'Reilly SY (1997) Multiple sources for basaltic rocks from Dubbo, eastern Australia: geochemical evidence for plume—lithospheric mantle interaction. Chem Geol 136:33–54